International Journal of Photoenergy

Materials for Photoelectric and Electrooptical Conversion and Device Applications

Lead Guest Editor: Jingkun Fang
Guest Editors: Liang Chu and Waqar Ahmad

Materials for Photoelectric and Electrooptical Conversion and Device Applications

International Journal of Photoenergy

Materials for Photoelectric and Electrooptical Conversion and Device Applications

Lead Guest Editor: Jingkun Fang
Guest Editors: Liang Chu and Waqar Ahmad

Chief Editor

Academic Editors

Contents

Hindawi
International Journal of Photoenergy
Volume 2019, Article ID 1069308, 7 pages
https://doi.org/10.1155/2019/1069308

Research Article

The Optimized Thickness of Silver Doping on CdS/CdSe for Quantum Dot-Sensitized Solar Cell

Ha Thanh Tung[1] **and Dang Huu Phuc**[2,3]

[1]*Institute of Research and Development, Duy Tan University, Da Nang, Vietnam*
[2]*Laboratory of Applied Physics, Advanced Institute of Materials Science, Ton Duc Thang University, Ho Chi Minh City, Vietnam*
[3]*Faculty of Applied Sciences, Ton Duc Thang University, Ho Chi Minh City, Vietnam*

Correspondence should be addressed to Dang Huu Phuc; danghuuphuc@tdtu.edu.vn

Received 14 June 2019; Revised 14 October 2019; Accepted 27 November 2019; Published 29 December 2019

Guest Editor: Jingkun Fang

Overall, CdSe:Ag^+ quantum dots were prepared by the successive ionic layer absorption and reaction method using two solutions: mixing molar concentrations of 0.003 mM $AgNO_3$ and a $Cd(CH_3COO)_2{\cdot}2H_2O$ anion to make solution 1 and 2.27 g Se powder and 0.6 M Na_2SO_3 were dissolved in 100 ml deionized water, solution 2. The FTO was coated with TiO_2 nanoparticles and then was dipped in both solutions, which created a FTO/TiO_2/CdSe:Ag^+ photoanode with a thickness of 1 layer to 4 layers. The layers of the CdSe:Ag^+ film show an effect on the morphology, crystalline structure, optical properties, and photovoltaic through optical and photovoltaic measurements. Finally, the performance of the device based on a FTO/TiO_2/CdSe:Ag^+ photoanode with the different thickness increased significantly to exactly 3.96%. Moreover, in the pattern of an explanation of the optical and photovoltaic properties of materials, we use Tauc's theory to determine the band gap, the conduction band, and the valence band.

1. Introduction

Quantum dot-sensitized solar cells (QDSSCs) are prominently becoming as a dye sensitized for the 3rd generation solar cells due to low cost fabrication technology, high photostability, the controlled sizes [1], higher absorption coefficient [2], and the multiple exciton generation [3]. However, the QDSSCs have reached approximately 13% performance, which is lower than the theory limits [4]. Recently, plenty of quantum dots (QDs) like CdS, CdSe, CdTe [5], and PbS [6] have been widely applied in the QDSSCs because of their unique properties [7]. It is noticeable that the CdS and CdSe QDs have attracted considerable interest due to their optical property stability [8], a higher conduction band (CB) than that of TiO_2 [9], low resistivity [10], and wide absorbed spectrum [11]. However, this result was still low compared with that of the dye-sensitized solar cells (DSSCs). The structure tandem as CdS/CdSe cosensitized was widely investigated due to their wide absorption spectrum, the shift of the absorption peak toward the visible region, and improvement of the CB of a cosensitized system compared to that of TiO_2 nanoparticles. The performance of this device based on a cosensitized system was approximately 4% [9], but it was still low compared to that of DSSCs, mostly due to the trapped and recombined TiO_2/QDs/electrolyte tripple interfaces [12].

In recent times, metal ions doped into the QDs can be replaced by single QDs and a cosensitized system to reduce achievable recombination [13–23] because it can be improved by charge collection and transfer process. In addition, metal ions are famous for its lowest resistance and large mobility. For example, Nguyen and colleagues achieved a performance of 4.22% as Cu^{2+} ion doped into CdSe QDs due to its good optical and magnetic properties as compared with each other [13]. The improved properties can be archived by doping metal in QDs like Ref [14, 15], [19–23] that can boost absorption of photons and the current density of devices.

In this work, Ag^+ ions were doped on CdSe QDs to study the properties of devices when the thickness of the CdSe:Ag^+ layers change while the molar concentration of Ag^+ ions doped on CdSe nanoparticles was optimized at 3% for the champion device. Moreover, resistance dynamic

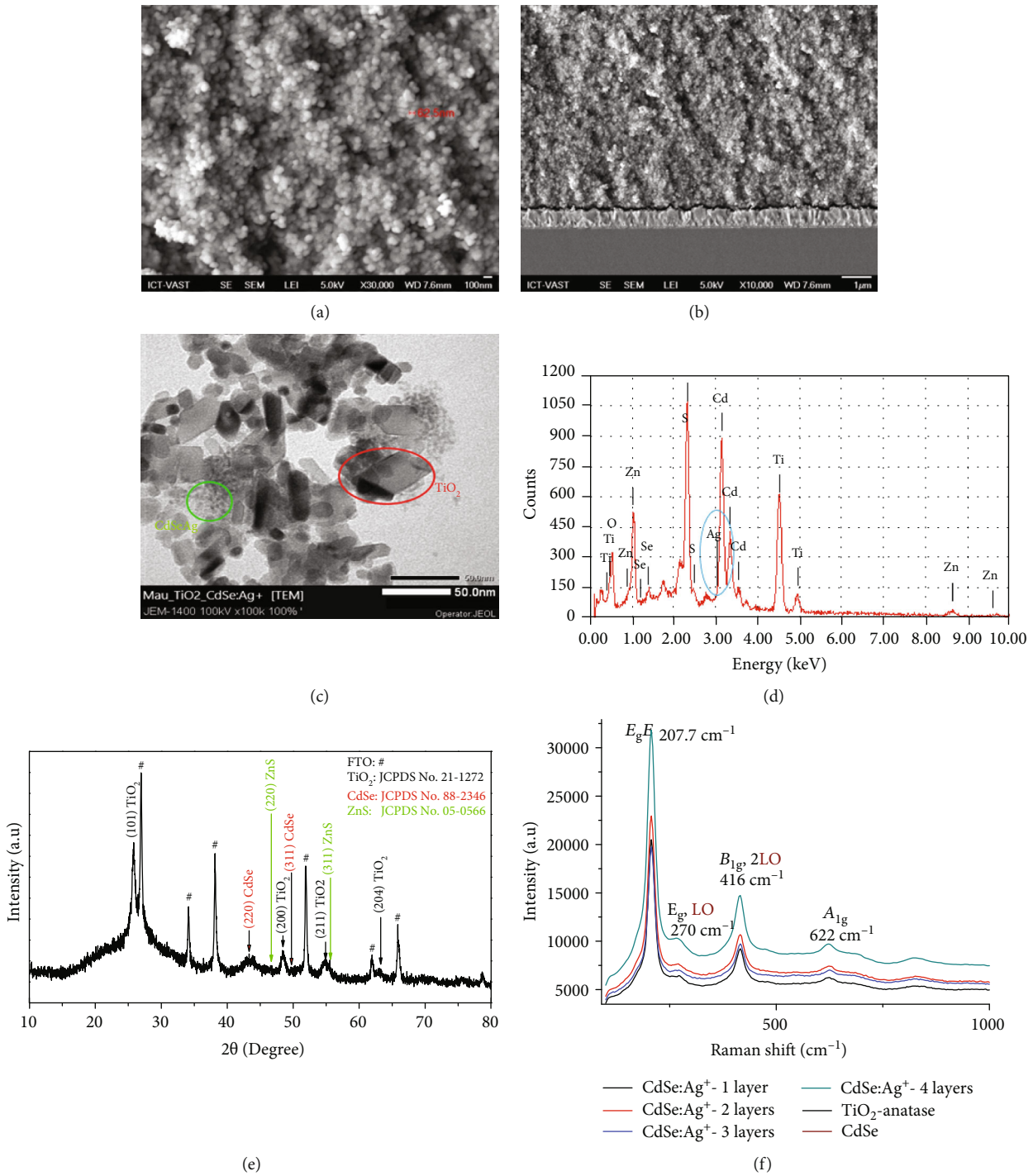

FIGURE 1: (a) FESEM image, (b) Cross-section, (c) TEM, (d) EDX spectrum, and (e) XRD pattern of TiO_2/CdSe:Ag^+(3%)/ZnS and (f) the Raman spectrum of photoanode with the different thickness.

was determined from an experiment J-V curve compared with that of electrochemical impedance spectra.

2. Experiment

2.1. Materials. Na_2SO_3, NaOH, $Cd(CH_3COO)_2{\cdot}2H_2O$, $Zn(NO_3)_2$, $Na_2S{\cdot}9H_2O$, methanol, Se powder, $TiCl_4$, and $AgNO_3$ were bought from Merck, and the fluorine-doped tin oxide was bought from Dyesol.

2.2. Preparation. TiO_2 paste was purchased from Dyesol in Australia with 20 nm sized average. The fluorine-doped tin oxide (FTO) was coated with TiO_2 layers by doctor blade and then heated to 400°C for 5 minutes, 450°C for 5 minutes, 490°C for 5 minutes, and 500°C for 30 minutes [24]. It was

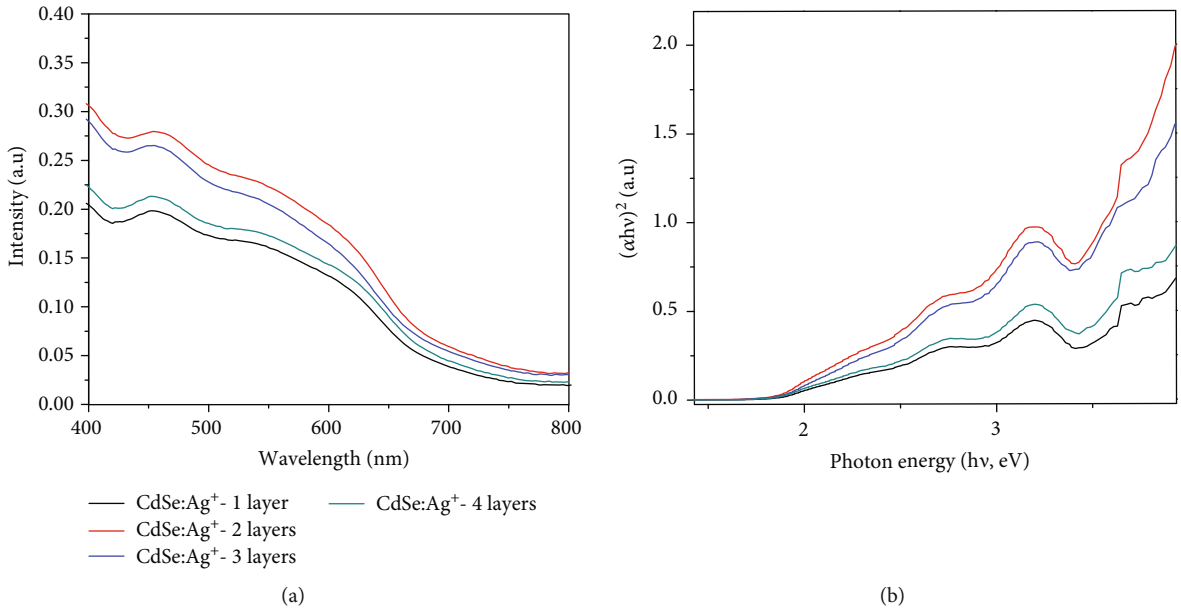

Figure 2: (a) UV-Vis spectra and (b) $(\alpha h\nu)^2$ vs. $(h\nu)$ curves of TiO_2/CdSe:Ag^+ with thickness from 1 layer to 4 layers.

then immersed in 40 mM $TiCl_4$ for 30 minutes at 70°C. Finally, the postheating treatment of TiO_2 film was carried out at 500°C for 30 minutes.

The TiO_2/CdSe:Ag^+ film: the TiO_2 film was dipped into a Cd^{2+} solution (molar concentrations of 0.001 mM, 0.002 mM, 0.003 mM, 0.004 mM, and 0.005 mM of $AgNO_3$ were mixed) and 0.5 M Cd^{2+} solution (13.3 g $Cd(CH_3COO)2{\cdot}2H_2O$ was dissolved in 100 ml ethanol) for 5 minutes, rinsed 3 times with ethanol, and dried in the air. It was then dipped into Se^{2+} ions (2.27 g Se powder, 0.6 M Na_2SO_3 were dissolved in 100 ml deionized water and added 5 ml NaOH 1 M). Finally, we got 0.3 M Se^{2+} solution at 50°C for 5 minutes, rinsed 3 times with deionized water for 1 minute, which was noticed one cycle. This process was repeated a total of 3 times SILAR.

The coated ZnS passivation: the TiO_2/CdSe:Ag^+ film was dipped in a mix of 0.2 M $Zn(NO_3)_2$ with deionized water for 1 min and rinsed with deionized water to remove ligands. Nextly, it was dipped in a solution of 0.2 $Na_2S{\cdot}9H_2O$ and methanol for 1 minute and rinsed with methanol to get a 1 cycle of SILAR. This process was repeated a total of 3 times SILAR. The detailed preparation process of electrolyte and counter electrode is listed in Ref [13].

2.3. Characterization. The scanning electron microscopy (SEM) with a JEOL 7500F high-resolution scanning electron microscope was used to determine the morphology of the films. Their characteristic and structure were confirmed using an X-ray diffractometer (Philips, PANalytical X'Pert, CuKα radiation), and optical properties are recorded by using a JASCO V-670. The J-V curves were measured (2400 Series SourceMeter, Keithley Instruments) under simulated AM 1.5 G sunlight at 100 mW·cm^{-2}. The active area of the solar cell measured under AM 1.5 G is 0.192 cm^2. The J-V scans were measured forward bias at a scan rate of 5 mV·s^{-1}. The electrochemical impedance spectroscopy (EIS) Series G 750 was measured under dark conditions at a forward bias of 0.75 V within the frequency range of 100 kHz to 0.1 Hz.

Table 1: The parameters of CdSe:Ag^+ films are determined using Tauc plots and UV-Vis spectra.

Samples	E_g (eV)	X (eV)	CB (eV)	VB (eV)
CdSe	2.16	5.102	-4.065	-6.225
CdSe:Ag^+ (1 layer)	2.0	5.102	-3.766	-5.766
CdSe:Ag^+ (2 layers)	1.96	5.102	-3.786	-5.746
CdSe:Ag^+ (3 layers)	1.96	5.102	-3.786	-5.746
CdSe:Ag^+ (4 layers)	1.95	5.102	-3.791	-5.741

3. Results and Discussion

In order to determine the morphology of the films, we used the FE-SEM images and cross-sectional of the previous paper. The result shows that the porous TiO_2 nanoparticles look like a sphere and the size average of 62.5 nm and thickness of the TiO_2/CdSe:Ag^+ were about 13 μm (Figure 1(b)) [24]. This result is also confirmed by TEM (shown in Figure 1(c)). The CdSe:Ag^+ nanoparticles in the film were not observed in the FE-SEM, but they can be clearly seen from TEM image. The average size of CdSe:Ag^+ nanoparticles was determined from Figure 1(c) approximately several nanomet. Moreover, the EDX spectrum of the photoelectrode was recorded in Figure 1(d). It is immediately obvious that the peak at 3 keV can be assigned to the characteristic of Ag^+ ions. The result shows that Ag^+ ions would be doped in CdSe QDs and effected on the photovoltaic. The typical XRD pattern of the photoelectrode was obtained in a vacuum environment at 200°C with the molar atomic of Ag^+ ion and CdSe QDs (3%) (shown in Figure 1(e)). The XRD pattern was recorded many diffraction peaks in a 2θ range

Table 2: The values of J-V curves and EIS with thickness from 1 layer to 4 layers.

QDSSCs	J_{SC} (mA/cm^2)	FF	V_{OC} (V)	η (%)	R_S (Ω)	R_{ct1} (Ω)	R_{ct2} (Ω)	τ_n (ms)	C_μ (μF)
CdSe:Ag$^+$ (1 layer)	7.46	0.44	0.38	1.22	21.29	30.77	18.92	2.38	12.25
CdSe:Ag$^+$ (2 layers)	15.36	0.41	0.50	3.96	21.3	46.54	26.94	6.86	72.66
CdSe:Ag$^+$ (3 layers)	12.22	0.42	0.44	2.83	24.34	193.1	81.46	5.19	86.72
CdSe:Ag$^+$ (4 layers)	9.89	0.46	0.47	2.11	19.44	293.5	82.6	5.51	39.70

from the 20° to 70°, which exhibits the structure of materials. By comparing the observed XRD patterns for the prepared film, Figure 1(e) shows the characteristic peaks of CdSe QDs, which correspond to the standard JCPDS card No. 88-2346 for the zinc blende structure and standard JCPDS card No. 05-0566 for the cubic phase of ZnS passivation. This result is consistent with that observed in the zinc blende phase [25, 26]. Figure 1(f) for the Raman spectrum of the completed QDSSCs with thickness between 1 layer and 4 layers always gives information about the TiO_2 anatase modes at 207.7 cm^{-1}, 416 cm^{-1}, and 622 cm^{-1} positions [27] and the TiO_2/CdSe:Ag$^+$ cubic at 207.7 cm^{-1}, 270 cm^{-1}, 416 cm^{-1}, and 622 cm^{-1} positions. All peaks shifted toward the high frequency because of the strengthening CdSe:Ag$^+$-TiO_2 associate as in those of CdSe-TiO_2 associate.

To research the effect of thickness on optical properties of TiO_2/CdSe:Ag$^+$ films, we use the UV-Vis spectra. We can see the differences from Figure 2(a) such as: while the thickness varied from 1 layer to 4 layers, the diagram describes an increase absorption intensity and shift of the absorption peak toward long wave because of Ag$^+$ trapping dopant inside the band gap of CdSe QDs [28–31]. Figure 2(b) shows the Tauc plots of CdSe:Ag$^+$ layers, and its parameters are shown in Table 1. The E_g of CdSe:Ag$^+$ nanoparticles decreased from 2.0 eV for 1-layer photoelectrode to 1.95 eV for 4-layer photoelectrode. This result shows that there was a strong influence of the thickness on the E_g of CdSe:Ag$^+$ film [32].

In order to study the photovoltaic characteristic, we conducted a set of the QDSSCs with different thickness (an active area of 0.38 cm^2) from 1 layer to 4 layers, and their parameters are listed in Table 2. When doping, open circuit parameters, short circuit currents, and efficiency are increased because the CB level of CdSe:Ag$^+$ layers raised higher than that of TiO_2 nanoparticles (listed in Table 1 and see in Figure 3) [24]. In the same optical properties, while 1.22% of performance for CdSe:Ag$^+$ 1 layer was recorded, the performance of devices for CdSe:Ag$^+$ 2 layers was sharply raised, at 3.96%. On the other hand, the performance of QDSSCs for CdSe:Ag$^+$ 2 layers and CdSe:Ag$^+$ 4 layers, which was recorded at 3.96% and 2.11%, respectively. It is obvious that the concentration impurities affect the properties of CdSe nanoparticles. Briefly, the highest performance was approximately 3.96%, corresponding to 3% of Ag$^+$ concentrations and 2 layers of CdSe:Ag$^+$ film. Figure 4 shows data on the CB and the VB of TiO_2 semiconductor and CdSe:Ag$^+$ nanoparticles; some parameters are referenced from Ref [33, 34]. Generally, the charges are not easy to transfer from the CB of QDs to TiO_2 oxide because -4.5 eV of the CB level for CdSe bulk was slightly lower than -4.3 eV of the CB level for TiO_2

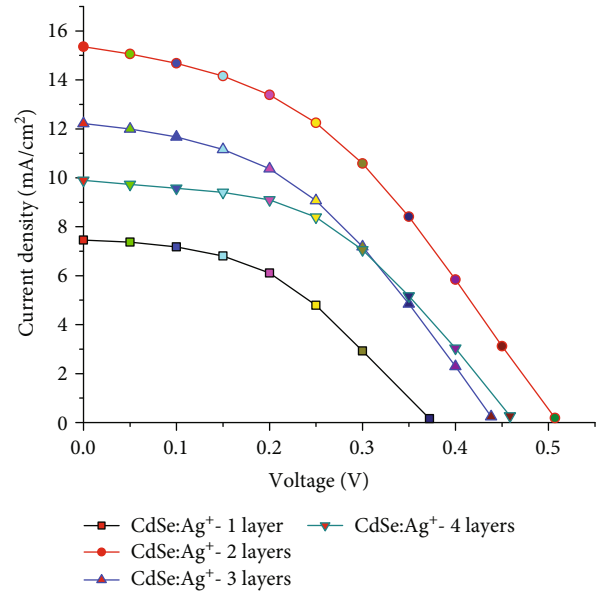

Figure 3: Photocurrent density-voltage (J-V) curves of QDSSCs with different thickness from 1 layer to 4 layers.

semiconductor bulk [22]. Therefore, in this work, Ag$^+$ ion was doped on CdSe nanoparticles to improve the conduction band and the absorption spectra. The graph gives information about the conduction band, bandgap, and valence band of CdSe:Ag$^+$ nanoparticles, which was calculated from Tauc's theory. -4.102 eV of the CB level for CdSe nanoparticles 1 layer and -3.786 eV of the CB level for CdSe nanoparticles 4 layers raised higher than those of the CB of TiO_2 nanoparticles (Figure 3). Finally, the charges can be easily removed from QDs to TiO_2. That is why the conversion efficiency and current density for device champion is high, at 3.96% and at 15.36 mA, respectively.

The EIS curves were used to determine the resistance dynamic in the QDSSCs (shown in Figure 5(b)) with different layers; the parameter values are shown in Table 2. Generally, there are two semicircles in the EIS curve, one small semicircle at high frequency of the resistance through polyelectrolyte/Cu_2S surface (R_{ct1}) and one large semicircle at low frequency of the diffuse resistance through TiO_2 film and TiO_2/CdSe:Ag$^+$ surface (R_{ct2}) [35]. In the recorded EIS curve, the fit process used Nova software to determine the parameters as the resistances (R_{ct1} and R_{ct2}), the capacitance (C_μ), and the lifetime (τ_n). The formulas of the lifetime and the capacitance are determined by $\tau_n = 1/(2\pi f_{min})$, and $C_\mu = \tau_n/R_{ct2}$ (shown in Table 2). Overall, Table 2 shows data

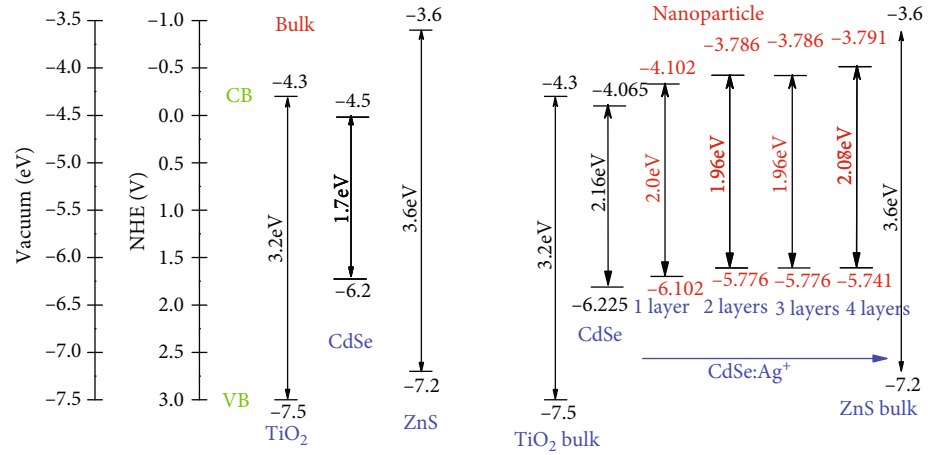

Figure 4: A schematic diagram for the band alignment in bulk materials and TiO_2/CdSe:Ag^+ photoanode.

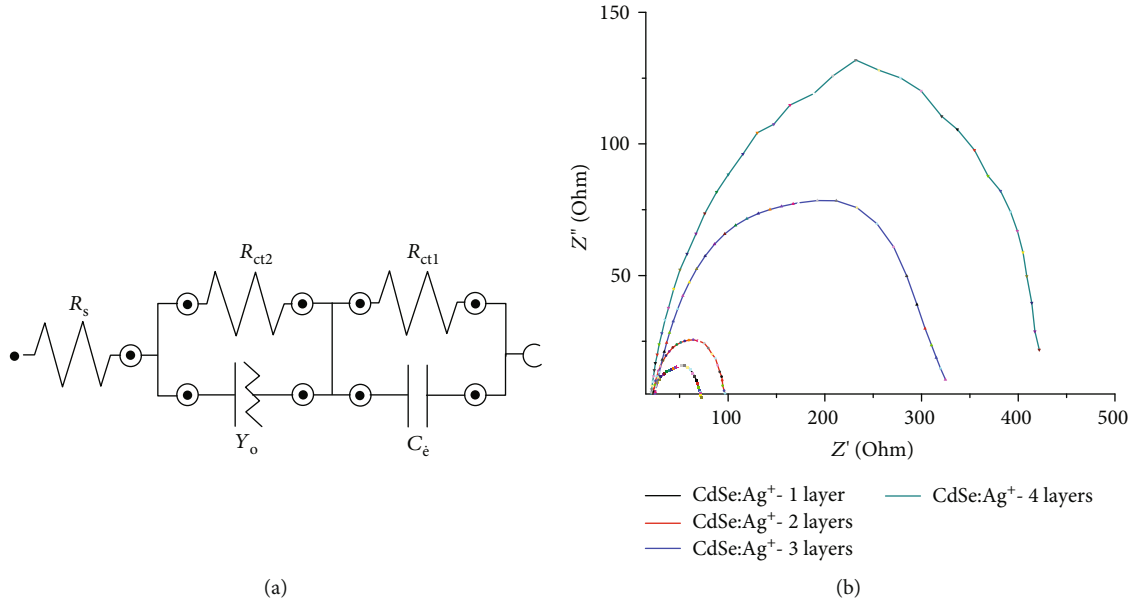

Figure 5: (a) The circuit diagram of devices and (b) Nyquist plots of QDSSCs with the different layers.

on the proportion of the device based on TiO_2/CdSe:Ag^+ photoelectrodes with the thickness of 1 layer to 4 layers, which affects the dynamic parameters of the photovoltaic properties. While the capacitance and lifetime of the excited charge was higher, the 293.5 Ω of R_{ct1} for CdSe:Ag^+ 4-layer photoelectrode and 82.6 Ω of R_{ct2} for CdSe:Ag^+ 4-layer photoelectrode were always higher than those of R_{ct1} and R_{ct2} for CdSe:Ag^+ 1-layer photoelectrode, at 30.77 Ω and 18.92 Ω, respectively [34]. Briefly, the improvement of energy band structure of CdSe nanoparticles as raising the conduction band reduces recombination and trapping surfaces, shifting the absorption spectra toward longwave due to the Ag^+ dopant, which appeared inside the band gap of CdSe nanoparticles. This result is also consistent with the results of Ref [33, 34, 36–38].

4. Conclusions

In conclusion, the device based on TiO_2/CdSe:Ag^+ photoanode with cycles changing from 1 to 4 was successfully prepared using the SILAR method with the obtaining highest efficiency of 3.96%. This result was also confirmed by the corporation of Ag^+ ion in photoelectrode, the changed sizes of QDs. The increase of the CB of the CdSe:Ag^+ QDs was caused by improvement of the performance. We also optimized the optical (E_g and lifetime τ), photovoltaic, and electrochemical properties through the optimized thickness of CdSe:Ag^+ films, thereby raising the efficiency of 3.96%. In order to compare with each other, we determined the values of dynamic resistances by EIS (R_s, R_{ct1}, R_{ct2}, and C_μ).

Data Availability

The analysis data used to support the findings of this study are included within the article. The supplementary material data used to support the findings of this study are included within the supplementary information files.

Conflicts of Interest

The authors declare no competing interests.

Acknowledgments

The authors would like to thank University of Science, VNU-HCM, Vietnam.

Supplementary Materials

Supplemental Figure 1: (a) FESEM image, (b) Cross-section, and (c) XRD pattern of TiO_2/CdSe:Ag+(3%)/ZnS and (d) the Raman spectrum of QDSSCs with the different thickness. The morphology of preparing as-photoelectrodes with 3% doping concentration could be obtained from FE-SEM. In addition, the compositions and structure of films could be investigated from EDX and Raman spectra. In general, this is the main data sets, which provided all information about the morphology, sizes, thickness of a sandwich layer, and structure of preparing as-photoelectrodes. Supplemental Figure 2: (a) UV-Vis spectra and (b) $(\alpha h\nu)2$ vs. $(h\nu)$ curves of TiO_2/CdSe:Ag+ with thickness from 1 layer to 4 layers. This is the supplementary material, which supports for us to determine the band gap of sample as getting the peak of UV-Vis spectra, in particular, calculate the conduction band and valence band of material. Supplemental Figure 3: photocurrent density-voltage (J-V) curves of QDSSCs with different thickness from 1 layer to 4 layers. The performance of the quantum dot-sensitized solar cells could be obtained from the photocurrent density-voltage curves. This results support for the discussion from the electrochemical impedance spectra. Supplemental Figure 5: Nyquist plots of QDSSCs with the different layers. The data set obtained from the electrochemical impedance spectra such as Nyquist curves and Bode phase. They used to determine resistance dynamic, lifetime, and capacitances of the photoelectrodes to correlate with the shift of excited electrons from quantum dots to TiO_2 nanoparticles, the diffusion of electrons. *(Supplementary Materials)*

References

[1] Z. A. Peng and X. Peng, "Formation of high-quality CdTe, CdSe, and CdS nanocrystals using CdO as precursor," *Journal of the American Chemical Society*, vol. 123, no. 1, pp. 183-184, 2001.

[2] M. C. Beard, "Multiple exciton generation in semiconductor quantum dots," *Journal of Physical Chemistry Letters*, vol. 2, no. 11, pp. 1282–1288, 2011.

[3] E. H. Sargent, "Infrared quantum dots," *Advanced Materials*, vol. 17, no. 5, pp. 515–522, 2005.

[4] S. Jiao, J. Du, Z. Du et al., "Nitrogen-doped mesoporous carbons as counter electrodes in quantum dot sensitized solar cells with a conversion efficiency exceeding 12%," *Journal of Physical Chemistry Letters*, vol. 8, no. 3, pp. 559–564, 2017.

[5] X. Shen, J. Jia, Y. Lin, and X. Zhou, "Enhanced performance of CdTe quantum dot sensitized solar cell *via* anion exchanges," *Journal of Power Sources*, vol. 277, pp. 215–221, 2015.

[6] A. N. Jumabekov, T. D. Siegler, N. Cordes et al., "Comparison of solid-state quantum-dot-sensitized solar cells withex Situandin SituGrown PbS quantum dots," *The Journal of Physical Chemistry C*, vol. 118, no. 45, pp. 25853–25862, 2014.

[7] J. Duan, Q. Tang, B. He, and L. Yu, "Efficient In_2S_3 Quantum dot–sensitized Solar Cells: A Promising Power Conversion Efficiency of 1.30%," *Electrochimica Acta*, vol. 139, pp. 381–385, 2014.

[8] L. Li, X. Zou, H. Zhou, and G. Teng, "Cu-Doped-CdS/In-Doped-CdS Cosensitized Quantum Dot Solar Cells," *Journal of Nanomaterials*, vol. 2014, Article ID 314386, 8 pages, 2014.

[9] Y. L. Lee and Y. S. Lo, "Highly Efficient Quantum-Dot-Sensitized Solar Cell Based on Co-Sensitization of CdS/CdSe," *Advanced Functional Materials*, vol. 19, no. 4, pp. 604–609, 2009.

[10] R. Mendoza-Pérez, J. Sastre-Hernández, G. Contreras-Puente, and O. Vigil-Galán, "CdTe solar cell degradation studies with the use of CdS as the window material," *Solar Energy Materials and Solar Cells*, vol. 93, no. 1, pp. 79–84, 2009.

[11] S. S. Liji Sobhana, M. Vimala Devi, T. P. Sastry, and A. B. Mandal, "CdS quantum dots for measurement of the size-dependent optical properties of thiol capping," *Journal of Nanoparticle Research*, vol. 13, no. 4, pp. 1747–1757, 2011.

[12] M. Abdellah, R. Marschan, K. Žídek et al., "Hole trapping: the critical factor for quantum dot sensitized solar cell performance," *Journal of Physical Chemistry C*, vol. 118, no. 44, pp. 25802–25808, 2014.

[13] T. P. Nguyen, T. T. Ha, T. T. Nguyen, N. P. Ho, T. D. Huynh, and Q. V. Lam, "Effect of Cu^{2+} ions doped on the photovoltaic features of CdSe quantum dot sensitized solar cells," *Electrochimica Acta*, vol. 282, pp. 16–23, 2018.

[14] F. Zhuge, X. Li, X. Gao, X. Gan, and F. Zhou, "Synthesis of stable amorphous Cu_2S thin film by successive ion layer adsorption and reaction method," *Materials Letters*, vol. 63, no. 8, pp. 652–654, 2009.

[15] S.-Q. Fan, R.-J. Cao, Y.-X. Xi, M. Gao, M.-D. Wang, and D.-H. Kima, "CdSe quantum dots as co-sensitizers of organic dyes in solar cells for red-shifted light harvesting," *Journal of Optoelectronics and Advanced Materials*, vol. 10, pp. 1027–1033, 2009.

[16] B. Fang, M. Kim, S. Q. Fan et al., "Facile synthesis of open mesoporous carbon nanofibers with tailored nanostructure as a highly efficient counter electrode in CdSe quantum-dot-sensitized solar cells," *Journal of Materials Chemistry*, vol. 21, no. 24, pp. 8742–8748, 2011.

[17] J. Fang, J. Wu, X. Lu, Y. Shen, and Z. Lu, "Sensitization of nanocrystalline TiO_2 electrode with quantum sized CdSe and ZnT_cP_c molecules," *Chemical Physics Letters*, vol. 270, no. 1-2, pp. 145–151, 1997.

[18] G. Chmid, *Nanoparticles: From Theory to Application*, John Wiley & Sons, 2014.

[19] G. Hodes, A. Albu-Yaron, F. Decker, and P. Motisuke, "Three-dimensional quantum-size effect in chemically deposited cadmium selenide films," *Physical Review B*, vol. 36, no. 8, pp. 4215–4221, 1987.

[20] S. Giménez, I. Mora-Seró, L. Macor et al., "Improving the performance of colloidal quantum-dot-sensitized solar cells," *Nanotechnology*, vol. 20, no. 29, p. 295204, 2009.

[21] V. Gonzalez-Pedro, X. Xu, I. Mora-Sero, and J. Bisquert, "Modeling high-efficiency quantum dot sensitized solar cells," *ACS Nano*, vol. 4, no. 10, pp. 5783–5790, 2010.

[22] M. Gratzel, "Photoelectrochemical cells," *Nature*, vol. 414, no. 6861, pp. 338–344, 2001.

[23] M. Gratzel, "Dye-sensitized solar cells," *Journal of Photochemistry and Photobiology C: Photochemistry Reviews*, vol. 4, no. 2, pp. 145–153, 2003.

[24] H. T. Tung, D. Van Thuan, J. H. Kiat, and D. H. Phuc, "Ag+ ion doped on the CdSe quantum dots for quantum-dot-sensitized solar cells' application," *Applied Physics A*, vol. 125, no. 8, 2019.

[25] S. Reghuram, A. Arivarasan, R. Kalpana, and R. Jayavel, "CdSe and CdSe/ZnS quantum dots for the detection of C-reactive protein," *Journal of Experimental Nanoscience*, vol. 10, no. 10, pp. 787–802, 2014.

[26] C. Zhai, H. Zhang, N. du et al., "One-pot synthesis of biocompatible CdSe/CdS quantum dots and their applications as fluorescent biological labels," *Nanoscale Research Letters*, vol. 6, no. 1, 2010.

[27] J. Y. Kim, S. B. Choi, J. H. Noh et al., "Synthesis of CdSe-TiO_2 nanocomposites and their applications to TiO_2 sensitized solar cells," *Langmuir*, vol. 25, no. 9, pp. 5348–5351, 2009.

[28] S. B. Singh, M. V. Limaye, N. P. Lalla, and S. K. Kulkarni, "Copper-ion-induced photoluminescence tuning in CdSe nanoparticles," *Journal of Luminescence*, vol. 128, no. 12, pp. 1909–1912, 2008.

[29] B. B. Srivastava, S. Jana, and N. Pradhan, "Doping Cu in Semiconductor Nanocrystals: Some Old and Some New Physical Insights," *Journal of the American Chemical Society*, vol. 133, no. 4, pp. 1007–1015, 2011.

[30] M. P. A. Muthalif, Y. S. Lee, C. D. Sunesh, H. J. Kim, and Y. Choe, "Enhanced photovoltaic performance of quantum dot-sensitized solar cells with a progressive reduction of recombination using Cu-doped CdS quantum dots," *Applied Surface Science*, vol. 396, pp. 582–589, 2017.

[31] N. S. Karan, D. D. Sarma, R. M. Kadam, and N. Pradhan, *Journal of Physical Chemistry Letters*, vol. 1, no. 19, pp. 2863–2866, 2010.

[32] C. V. V. M. Gopi, M. Venkata-Haritha, S.-K. Kim, and H.-J. Kim, "A strategy to improve the energy conversion efficiency and stability of quantum dot-sensitized solar cells using manganese-doped cadmium sulfide quantum dots," *Dalton Transactions*, vol. 44, no. 2, pp. 630–638, 2015.

[33] K. Veerathangam, M. Senthil Pandian, and P. Ramasamy, "Photovoltaic performance of Pb-doped CdS quantum dots for solar cell application," *Materials Letters*, vol. 220, pp. 74–77, 2018.

[34] K. Veerathangam, M. S. Pandian, and P. Ramasamy, "Photovoltaic performance of Ag-doped CdS quantum dots for solar cell application," *Materials Research Bulletin*, vol. 94, pp. 371–377, 2017.

[35] O. Amiri, M. Salavati-Niasari, and M. Farangi, "Enhancement of Dye-Sensitized solar cells performance by core shell (organic=2-nitroaniline, PVA, 4-choloroaniline and PVP): Effects of shell type on photocurrent," *Electrochimica Acta*, vol. 153, pp. 90–96, 2015.

[36] D. H. Phuc and H. T. Tung, "Quantum dot sensitized solar cell based on the different photoelectrodes for the enhanced performance," *Solar Energy Materials and Solar Cells*, vol. 196, pp. 78–83, 2019.

[37] Y.-J. Shen and Y.-L. Lee, "Assembly of CdS quantum dots onto mesoscopic TiO2films for quantum dot-sensitized solar cell applications," *Nanotechnology*, vol. 19, no. 4, p. 045602, 2008.

[38] W. W. Yu, L. Qu, W. Guo, and X. Peng, "Experimental determination of the extinction coefficient of CdTe, CdSe, and CdS nanocrystals," *Chemistry of Materials*, vol. 15, no. 14, pp. 2854–2860, 2003.

Hindawi
International Journal of Photoenergy
Volume 2019, Article ID 3579587, 8 pages
https://doi.org/10.1155/2019/3579587

Research Article

Study on the Stability of Unpackaged CdS/CdTe Solar Cells with Different Structures

Guanggen Zeng,[1,2] **Xiaolan Liu**,[1] **Yubo Zhao**,[1] **Yuanmao Shi**,[1] **Bing Li**,[1] **Jingquan Zhang**,[1] **Lianghuan Feng**,[1] **and Qionghua Wang**[2]

[1]*College of Materials Science and Engineering, Sichuan University, Chengdu 610065, China*
[2]*College of Electronics and Information Engineering, Sichuan University, Chengdu 610065, China*

Correspondence should be addressed to Guanggen Zeng; yigezeng@sina.com.cn

Received 25 September 2019; Accepted 3 December 2019; Published 20 December 2019

Guest Editor: Liang Chu

In this work, the stability of unpackaged CdTe solar cells with different configurations was investigated according to the International Electrotechnical Commission IEC 61215-2016. The measurements of thermal cycling from -40°C to +85°C and 24-hour temperature cycling from -40°C to +85°C withstanding the effects of 20-hour penetration of 85°C were carried out in CdS/CdTe solar cells with structures of FTO/CdS/CdTe/Au, FTO/CdS/CdTe/back contact/Au, and FTO/MZO/CdS/CdTe/back contact/Au, respectively. The performances of these cells before and after the thermal aging experiments were investigated by using light and dark *I-V* together with *C-V*. The results reveal varied performance degradation before and after thermal aging in the cells with different structures. Among these, the most deteriorated device is the one without back contact (BC), whose efficiency decreased by 25.12% after thermal cycling accompanying an obvious roll-over phenomenon when forward bias was greater than open circuit voltage. On the contrary, the reduction in the efficiency was about 16.80% in the case cells with BC, and the roll-over phenomenon was not so significant. Furthermore, for the devices with optimized front contact of FTO/MZO, the thermal stability was improved obviously. Interestingly, short-circuit current density associated with the carrier concentration of cells remained relatively small variations compared with the change of V_{oc} and fill factor. All the results indicated that an efficient back contact layer and an optimized front electrode were the indispensable structural elements to attain high stabilization in the CdS/CdTe solar cells.

1. Introduction

The research on weather resistance of a solar cell is always time-consuming, expensive, and thus complicated. Therefore, it is necessary to accelerate the test process to study the stability and failure mechanism of the solar cell under thermal cycling, which is supposed to predict the actual evolution of solar cell performance without too long duration. This technique is of great importance in providing reliable indications for the device design and stability optimization of the solar cell. At present, the qualification tests of the International Electrotechnical Commission IEC 61215-2016 and IEC 61583 [1], such as visual inspection and thermal cycling test, are applied to all terrestrial flat plate module materials such as crystalline silicon and thin-film modules. The literature survey on degradation rates reported by Jordan et al. indicated that the qualification tests have been quite successful in identifying and eliminating module types that suffer high degradation rates early in their lifetime [2]. However, stability test experiments showed that standard device test results cannot be used to predict the service life of cell products [3]. Therefore, it is necessary to prioritize studying the factors that cause aging acceleration of a specific freshly fabricated cell in a lab.

A CdTe thin-film solar cell has attracted intensive research interests because CdTe has a direct band gap of 1.46 eV matching the energy of a solar spectrum and an absorption coefficient as high as 10^{-5} cm^{-1} meaning 90% of

visible light can be absorbed by CdTe with a thickness of 1 micron [4]. Although the CdTe solar cell with a new world conversion efficiency record of 22.1% has been fabricated successfully [5], there are still some key issues that need to be understood with respect to the changes in device performance operated in general open-air conditions, as defined in IEC 60721-2-1. Generally, the failure causes of the CdTe solar cell mainly come from the functional materials and device configuration, especially in thickness, grain boundaries, and internal defects of films [6–9]. On the other hand, the performance of a solar cell is closely related to the properties of the package process as well as the materials. For example, one representative packaging material, adhesive EVA (Ethylene+Vinyl+Acetate), is supposed to be corresponding to the possible failures that include delamination, air leakages, insulation failure, and package damage [10]. The manufacture of the CdS/CdTe solar cell includes at least 4 different processes, specifically including a high temperature process of cadmium telluride preparation, which means that the control of the quality of each layer and the characteristics of the interface is critical [11, 12]. Therefore, through in-depth study on the correlation between the aforementioned factors and the device performance in a certain duration under designated conditions, the degradation mechanisms of devices might be clarified effectively [11]. Currently, various methods have been developed to study the stability of the cadmium telluride solar cell, including theoretical simulations and practical tests [13–15]. For example, the stabilization was achieved to varying degrees using either light-soaking or dark-bias methods, and the existing IEC 61646 light-soaking interval might be appropriate for CdTe modules [16].

Current standard tests were employed to simulate the degradation properties of modules under outdoor operation conditions. However, the decomposed analysis after the stability test on packaged modules will be extremely difficult. Therefore, it is important to develop short-term experimental methods to verify the changes in the outdoor performance of devices without the package, and the conditions of these methods need to be adjusted accordingly to avoid unnecessary damages, such as humidity and insulation testing. So far, little research was involved in the stability of the CdTe solar cell under thermal cycling. With the change of thermal cycling from -40°C to +85°C, the cell will be repeatedly frosted and thawed, resulting in some complicated effects of thermal shock on the cell chip. For study on the stability of unpackaged devices by selecting the terms of the standard test, there should be targeted trade-offs to avoid introducing more uncertainties. In previous studies, we found that IEC thermal cycling test conditions were applicable to the unpackaged CdTe solar cell to a certain extent.

Based on the above analysis, the stabilization of CdS/CdTe solar cells with different structures was analyzed according to the International Standard IEC 61215-2016 test specifications in this work. These structures were depicted as the following: FTO/CdS/CdTe/Au corresponding to sample 1, FTO/CdS/CdTe/BC/Au corresponding to sample 2, and FTO/MZO/CdS/CdTe/BC/Au corresponding to sample 3, respectively. All the CdS/CdTe solar cells were subjected to the thermal cycling tests from -40°C ± 2°C to +85°C ± 2°C and 24-hour temperature cycle test with only 1 cycle from -40°C ± 2°C to +85°C ± 2°C under a constant relative humidity of 85%. The stability of cells with different structures has been investigated after thermal experiments by using the light and dark *I-V* and *C-V* test methods.

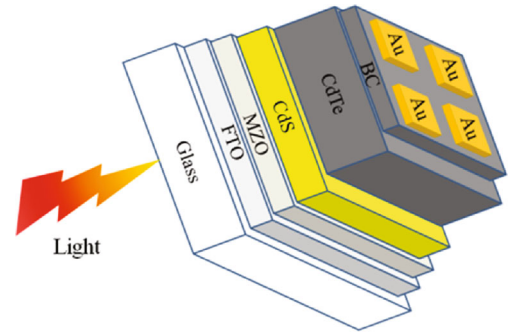

Figure 1: The structure of sample 3.

2. Experimental Procedure

In this work, CdS/CdTe heterojunction thin-film solar cells with different structures were fabricated as follows: the SnO_2:F (FTO) films coated on commercial glasses commonly used in our laboratory were selected as substrate, and ZnO:Mg was prepared by using magnetron sputtering technology as an optional buffer layer between FTO and CdS. A 50 nm thick CdS thin film was deposited by using the chemical bath deposition (CBD) technique at about 85°C, followed by the deposition of the CdTe film (~5 μm) by using the close-space sublimation (CSS) method for 4 minutes. The CSS chamber was initially evacuated to a pressure of 5×10^{-2} Pa, and a mixture of 99.999% pure argon and 99.999% oxygen (the oxygen partial pressure was 8%) was then charged into the chamber to maintain a pressure of 1 kPa. The space from substrate to source was 2 mm, and the source and substrate were simultaneously heated to about 650°C and 550°C, respectively. Afterwards, CdTe films were annealed for 30 minutes with a $CdCl_2$ source in a tube furnace preheated to 380°C under 1 atmospheric pressure of mixed N_2+O_2 gas (volume ratio 4 : 1). And then, ZnTe:Cu as the back contact layer was deposited by using the vacuum thermal evaporation technique after the CdTe film was etched by bromine methanol solution with a bromine concentration of 0.2% for 4 s. The ZnTe and Cu powders with high purity (99.999%) were used as evaporation sources with separate crucibles. Two quartz crystal monitors were employed to monitor the deposition rates of ZnTe and Cu on-line, respectively. Finally, unit cells with areas of 0.5 cm^2 were achieved by depositing a 100 nm thick gold electrode with a shadow mask. The structure schematic diagram of sample 3 was shown in Figure 1.

Aging tests including thermal cycling (from -40°C to +85°C with different cycles) and 24-hour temperature cycle with 1 cycle from -40°C to +85°C as shown in Figure 2 were carried out according to IEC 61215-2016 by using a climatic chamber produced by Hong Zhan Technology Co., Ltd. with a programmable temperature controller having an accuracy

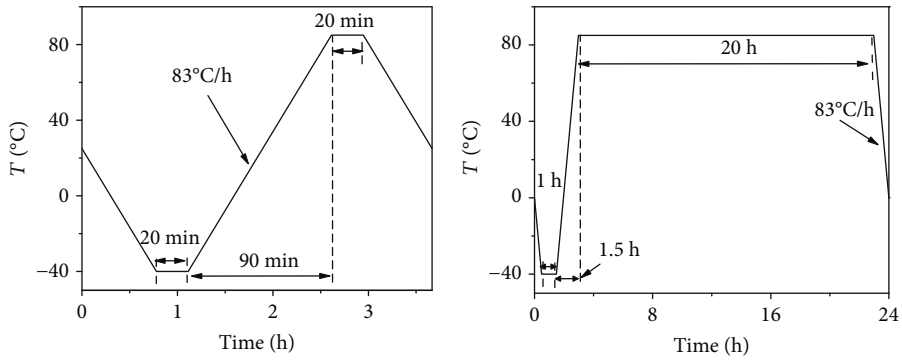

Figure 2: The profile of one cycle time: (a) thermal cycling and (b) 24-hour temperature cycle.

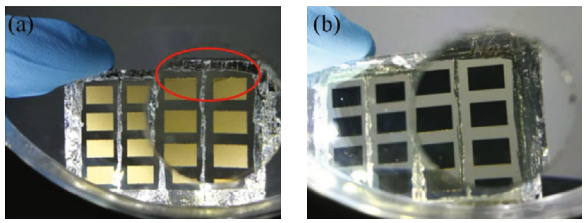

Figure 3: The visual inspection of front (a) and back (b) sides of cells (the view of the right area observed through convex lens) under 1000 lux of fluorescent light.

of ±2.0°C attached with a suitable temperature sensor to the front of the representative cell near the middle with means for circulating the air inside to improve the uniformity of the temperature field and minimize condensation on the devices during the test. Light *I-V* characteristics of CdTe solar cells were carried out by using a Solar Cell Tester (Gsola XJCM-9) under AM1.5 with light intensity of 1000 W/m^2 and temperature of 25°C according to IEC 60904-1 and IEC TS 61836, and dark *I-V* characteristics of all solar cells were performed at room temperature by Agilent 4155C. Meanwhile, *C-V* curves were obtained at room temperature via an Agilent 4155A with a test frequency of 1 MHz and scan bias range from -1 V to +1.5 V.

3. Results and Discussion

3.1. Thermal Cycling

3.1.1. Visual Inspection. In this section, the inspection was focused on the visual defects, such as warping, delamination, bubbles, scratches, and stains in cells under an illumination of no less than 1000 lux as defined in IEC 61215-1. Figure 3 shows the implementation of inspection. Before the demonstration of device performance, a laser was employed to etch and remove the films at the edge of the electrode to eliminate bypass collection of devices. Because of a relatively weak adhesion between the gold electrode and the ZnTe:Cu films, a peeling off at the edge of the back electrode usually occurred during the etching process, which was marked with a red circle in Figure 3(a). This defect seriously affected the current collection of the back electrode and cannot meet the specification of the test standard, so in the later device test, cells with partial electrode peeling off have been ignored. No other defects as mentioned above were found in the electrode of other cells. Figure 3(b) displays the back of cells through the glass side, and a uniform and dark black colour with no red or yellow spot, no scratch, or no damage can be observed, meaning that a uniform and complete cathode in the cell has been obtained.

3.1.2. Light I-V Characteristics. The accelerated thermal cycle tests were conducted on 16 unit cells with designated structures fabricated from one batch to determine the ability of them to withstand thermal mismatch, fatigue, and other stresses caused by repeated changes of temperature, as shown in Figure 3. After 100 thermal cycles, 5 cells from sample 1 failed and the reasons of the failure included the aforementioned electrode peeling off. As for the cells from sample 2 and sample 3, 2 cells of each group failed. The *I-V* curves of the representative cells before and after thermal cycling were shown in Figure 4. Note that for the cells that underwent thermal cycling, the *I-V* measurement was carried out after 1 hours' recovery time at 23°C.

From Figure 4, a roll-over phenomenon of current-voltage characteristics near the open circuit voltage of sample 1 can be observed obviously, which was due to a metal-semiconductor barrier caused by a nonohmic contact between CdTe and Au because of the work function of CdTe ~5.5 eV greater than that of most metals, including gold ~5.1 eV as the back electrode in this work [17]. As the number of thermal cycles increased, the fill factor (FF), short-circuit current (J_{sc}), and open circuit voltage (V_{oc}) of sample 1 kept declining. After 100 thermal cycles, FF, J_{sc}, and V_{oc} of cells from sample 1 decreased by 10.11%, 5.90%, and 11.48%, respectively, eventually resulting in a degradation in conversion efficiency (η) of 25.13% compared with the initial η as shown in Figure 5. No roll-over phenomenon near V_{oc} of sample 2 and sample 3 was perceived in Figures 4(b) and 4(c) under illumination. After 100 thermal cycles, FF, J_{sc}, and V_{oc} of sample 2 decreased by 8.2%, 4.1%, and 5.6%, respectively, resulting in a degradation in η of 16.80% as compared with the initial η while the corresponding parameters of sample 3 reduced by 6.2%, 7.1%, and 0.1%, respectively, accompanied by a 10.6%

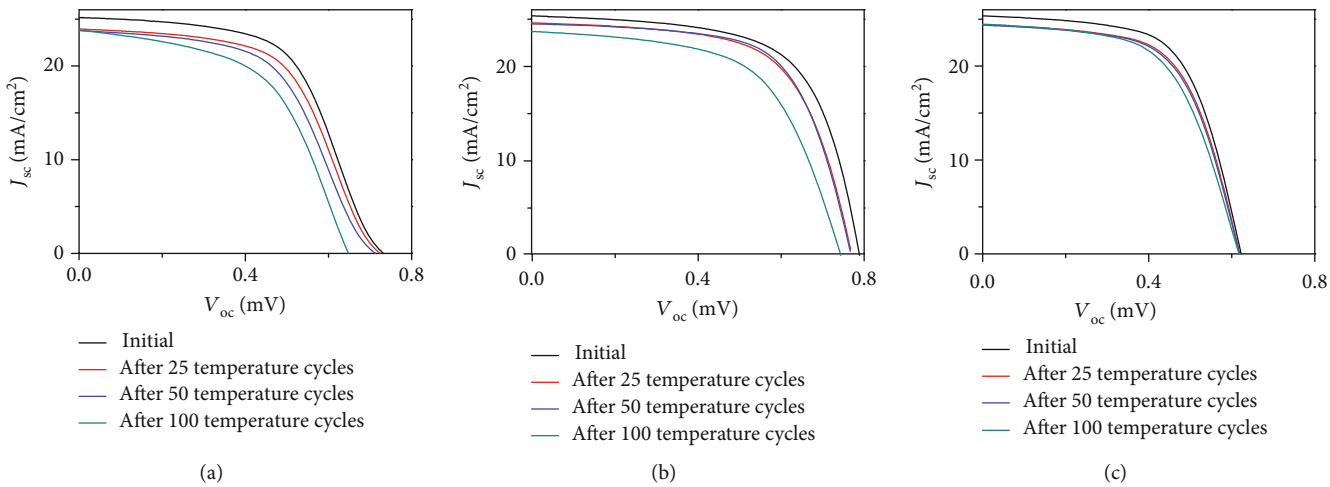

Figure 4: Comparison of light J-V curves of (a) sample 1, (b) sample 2, and (c) sample 3 before and after different cycles of thermal cycling.

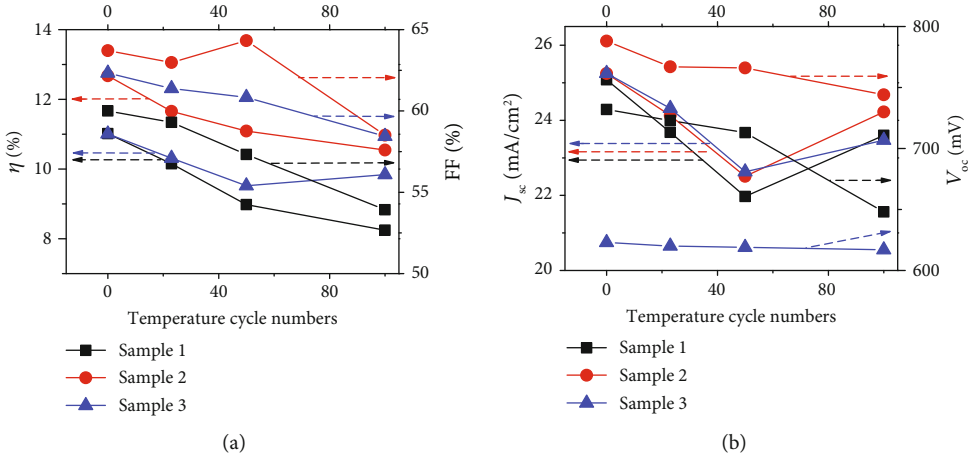

Figure 5: The photovoltaic parameters of cells as a function of thermal cycling numbers: (a) η and FF; (b) J_{sc} and V_{oc}.

reduction in conversion efficiency. The above changes in performances of sample 2 and sample 3, especially in series resistance, should be attributed to a good back contact ZnTe:Cu between CdTe and Au which can effectively reduce the contact barrier and eliminate the influence of the Schottky junction [18]. As MZO layer was introduced between FTO and CdS, the initial performance of sample 3 was lower than that of sample 2.

In our other work, the CdTe cell with conversion efficiency exceeding 16% has been achieved when introducing MZO as an optimized buffer layer [19]. In Kephart et al.'s report, MZO has completely replaced the window layer CdS with a further optimized structure [20]. However, in this work, in order to compare the stability of devices with different configurations, the thicknesses of the functional layers were kept the same and the device performance was therefore not optimized. Interestingly, the stability of sample 3 was superior, especially reflected by the almost unchanged V_{oc} after 100 thermal cycles. However, J_{sc} degradation of sample 3 was more severe close to 7.1% as compared to that of sample 2. This indicated that the MZO absorbed some of the photons which were supposed to be entering CdS/CdTe heterojunction and induced an extra barrier between FTO and CdS, which resulted in an increased electron reflection.

Meanwhile, the fluctuation of J_{sc} was much smaller than that of other parameters of all the samples. During the thermal cycling, the cooling process will cause obvious decrease in the minority carrier concentration, while as temperature increases, the short-circuit current increases moderately owing to an improvement of contact performance by alleviating the residual stress between the layers in the cell and an increase in lifetime and diffusion coefficient of photogenerated carriers. Furthermore, the reverse saturation current I_0 increased greatly with an increase of thermal cycling numbers as analyzed later, revealing that after a thermal cycle, the change of the carrier was irreversible. Therefore, a shift in the current-voltage curve of the cell was negligible, where the degradation in η of all cells exceeding 10% was not only related to the influence of the grain boundary on the diffusion of dopants, impurities, electromigration of charged atoms, and self-compensation effect during thermal cycling but also related to the water vapor in the environment that will enter the interior of unpackaged cells causing a considerable damage to CdS/CdTe heterojunction [12].

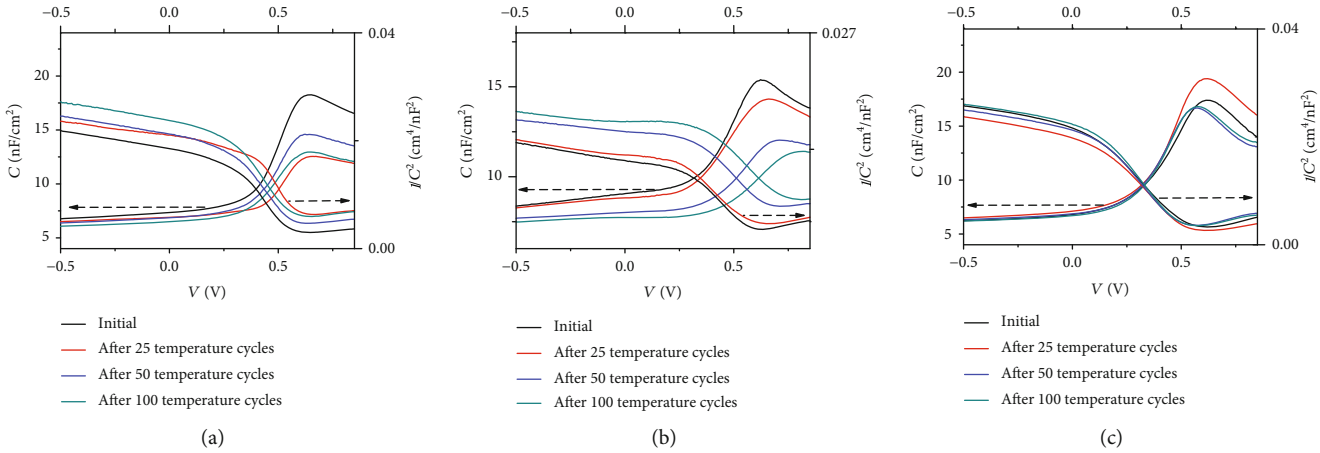

FIGURE 6: Comparison of C-V and C^{-2}-V curves before and after different cycles of thermal cycling: (a) sample 1, (b) sample 2, and (c) sample 3.

3.1.3. C-V Characteristics. As shown in Figure 6, the capacitance of the cell with the nonlinear characteristic increased obviously when forward bias was greater than 0.3 V, while the capacitance decreased when bias increased in the vicinity of V_{oc} (0.8 V), which correspond to an inversion region. The capacitance tended to be saturated when bias was less than 0.3 V, especially in reverse bias, assigned to an accumulation region. As the number of thermal cycles increased, the capacitance variation of sample 1 and sample 2 became significantly larger than that of sample 3, which was closely related to the change of the p-n junction region. The structure of the CdTe thin-film solar cell can be equated to a plate capacitor, and its physical properties such as doping concentration N_D, depletion region width X_D, and built-in electric field V_D can be explained by the C-V characteristic [21, 22].

Under the condition of depletion layer approximation, the barrier capacitance C_T of CdTe/CdS considered as an abrupt heterojunction is depicted as the following:

$$C_T = \frac{A\varepsilon_r\varepsilon_0}{X_D},$$
$$C_T = A\sqrt{\frac{\varepsilon_r\varepsilon_0 qN_D}{2(V_D - V)}}, \quad (1)$$

where A is the cell area, the relative dielectric constant ε_r of CdTe is about 9, and the vacuum permittivity ε_0 is 8.85×10^{-12} F/m. Simply change the above formula to get the following formula:

$$\frac{1}{C_T^2} = \frac{2V_D}{A^2\varepsilon_r\varepsilon_0 qN_D} - \frac{2V}{A^2\varepsilon_r\varepsilon_0 qN_D}. \quad (2)$$

Then, differentiate the above formula:

$$\frac{d\left(1/C_T^2\right)}{dV} = \frac{2}{A^2\varepsilon_r\varepsilon_0 qN_D}. \quad (3)$$

N_D and V_D can be obtained from the slope and intercept by fitting the straight line portion of the $1/C^2 \sim V$ relationship curve plotted in Figure 6 under a bias range of 0.4 V~0.6 V, respectively. All the values of X_D, N_D, and V_D were listed in Table 1.

These parameters of sample 1 and sample 2 were considerably different from those of sample 3. Taking the change of X_D at a forward bias of 0.6 V as an example, X_D of sample 1 increased by 45.45%, 23.63%, and 40.00% after 25, 50, and 100 cycles, respectively. Meanwhile, X_D of sample 2 and sample 3 increased by 7.69%, 27.69%, and 35.38% and -8.77%, 3.50%, and 3.50%, respectively. It was worth noting that N_D and V_D of the samples decreased as X_D increased after thermal cycles, and the change trend of N_D and V_D was basically the same as that of J_{sc} and V_{oc} described above, respectively, which means that the thermal shock has a significant effect on the minority carrier concentration and electric field strength inside p-n heterojunction.

3.1.4. Dark I-V Characteristics. Dark current was very small and relatively insensitive to variation at a bias less than 0.4 V, especially under reverse bias, while dark current increased exponentially as forward bias exceeding 0.4 V as depicted in Figure 7. However, significant differences in dark current variations of cells with different configurations can be observed clearly as a function of thermal cycling numbers. When forward bias was greater than 0.4 V, dark current of sample 1 rose rapidly with an inflection point defined as roll-over phenomenon at a bias around 0.6 V. As the number of thermal cycles increased, roll-over phenomenon became more obvious. However, the change of dark current of sample 2 was still small at a bias closed to 0.6 V, and no roll-over phenomenon of current can be observed even when bias increased to 0.8 V. For sample 3, its current had risen by a certain amplitude near 0.6 V, but a very small inflection point can be perceived at a bias exceeding 0.7 V. Furthermore, a relatively obvious roll-over phenomenon was presented after the number of thermal cycles increased to 100 times.

Table 1: Dark I-V and C-V parameters of samples before and after thermal cycling.

Sample	Experimental condition	A	J_0 (mA/cm^2)	X_D (μ)	N_D (10^{14} cm^{-3})	V_D (V)
1	Initial	2.10	2.59×10^{-11}	0.65	1.36	0.65
	After 25 temperature cycles	2.34	4.05×10^{-11}	0.70	1.29	0.60
	After 50 temperature cycles	3.01	1.786×10^{-10}	0.83	1.22	0.66
	After 100 temperature cycles	5.76	1.85×10^{-8}	0.88	1.28	0.66
2	Initial	1.98	8.55×10^{-12}	0.55	1.30	0.60
	After 25 temperature cycles	2.20	2.09×10^{-11}	0.80	1.24	0.74
	After 50 temperature cycles	2.22	4.7×10^{-11}	0.68	1.14	0.59
	After 100 temperature cycles	2.20	3.6×10^{-11}	0.77	1.24	0.68
3	Initial	2.12	3.52×10^{-11}	0.57	1.37	0.56
	After 25 temperature cycles	2.10	2.54×10^{-11}	0.52	1.32	0.52
	After 50 temperature cycles	2.14	3.84×10^{-11}	0.59	1.24	0.51
	After 100 temperature cycles	2.36	4.54×10^{-11}	0.59	1.27	0.53

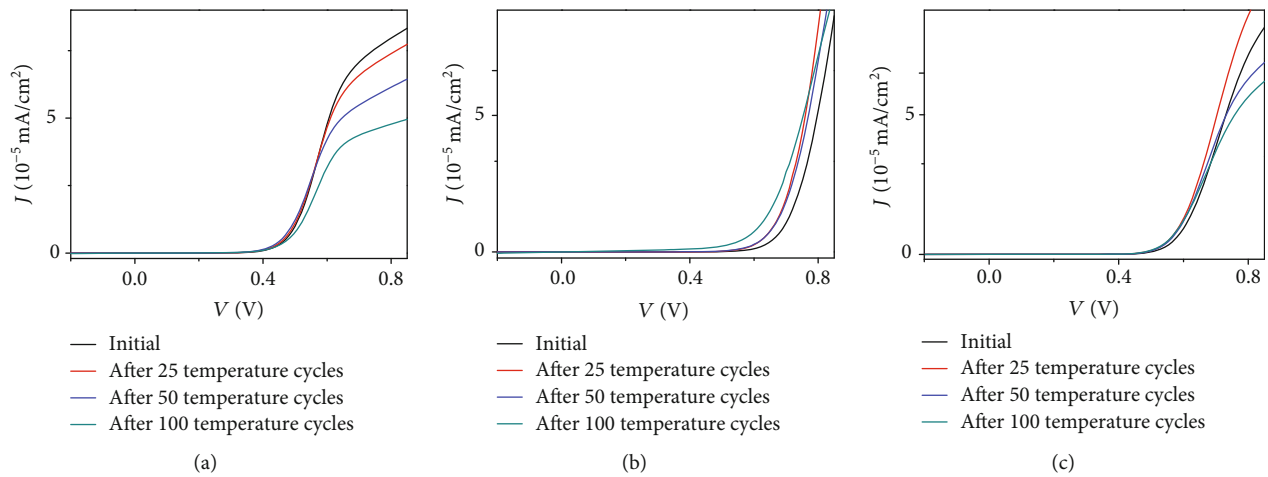

Figure 7: Comparison of dark current-voltage curves before and after different cycles of thermal cycling: (a) sample 1, (b) sample 2, and (c) sample 3.

The above changes might be analyzed by using the current-voltage equation of ideal p-n junction in the dark state described as follows:

$$I = I_0\left(e^{q(V-IR_s)/AKT} - 1\right) + \frac{V - IR_s}{R_{sh}}, \quad (4)$$

where I_0 is dark reverse saturation current, K is Boltzmann's constant, A is defined as the diode ideality factor representing the diffusion and recombination current components, R_s is series resistance, R_{sh} is shunt resistance, and in this work T is 298 K. Before thermal cycling, A of all samples was around 2.0 as listed in Table 1, indicating that the junction current was mainly composed of recombination current [23, 24]. After 100 cycles of thermal cycling, A of sample 1 increased to 5.76, indicating that the carrier transport has changed to the hot-electron emission mechanism. The dark reverse saturation current density J_0 of sample 1 increased by 3 orders of magnitude while that of sample 2 and sample 3 increased by 321% and 29%, respectively, meaning CdS/CdTe heterojunction was destroyed to some extent. The evolution of dark current was attributed to varying barrier height exposed by the change of R_s at the interface of the cell [25]. In this case, carriers needed extra energy to "climb" the barrier, resulting in a significant decrease in the amount of electrons which arrived at the back electrode by the hot-electron emission mechanism. Furthermore, when a back contact layer was introduced into devices, as shown in Figure 7(b), the roll-over phenomenon of sample 2 was well suppressed. While MZO was introduced as a buffer layer between FTO and CdS, J_0 of sample 3 remained a relatively small variation as the number of thermal cycling cycles increased, but a slight roll-over phenomenon can be perceived, which was due to an increase of R_s caused by MZO. These conclusions were consistent with the results discussed above.

Table 2: Light I-V parameters of samples before and after the 24-hour thermal cycle.

Sample	Experimental condition	η (%)	FF (%)	J_{sc} (mA/cm^2)	V_{oc} (mV)
1	Before	10.10	59.01	23.60	725
	After	8. 41	55.34	23.16	656
2	Before	11.60	63.44	24.12	758
	After	10.21	59.59	23.81	721
3	Before	10.89	62.62	24.13	721
	After	9.90	59.13	23.80	703

3.2. 24-Hour Temperature Cycle. The 24-hour temperature cycle test (1 cycle from -40°C to +85°C) was conducted on samples with the aforementioned structure, named as samples 1, 2, and 3, respectively, and the parameters derived from light I-V curves of these samples were listed in Table 2. After the 24-hour temperature cycle, FF, J_{sc}, V_{oc}, and η of sample 1 decreased by 6.2%, 1.8%, 9.5%, and 16.7%, respectively, and the corresponding parameters of sample 2 and sample 3 decreased by 6.1%, 1.3%, 4.9%, and 12.0% and 5.6%, 1.4%, 2.5%, and 9.1%, respectively. Compared to the change of other parameters of all samples, the variation of J_{sc} was very weak. The parameter variation of sample 3 was consistent with the results of the above thermal cycling experiments. This further verified that a back contact layer was critical to the stability of the CdS/CdTe solar cell, and a composite front electrode was also conducive to potentially improve cell stability.

4. Conclusion

In summary, the effects of thermal shock according to the IEC standard on the stability of the unpackaged CdTe solar cell with different structures were analyzed while the reasons of cell performance degradation were also discussed. The experimental results showed that there were significant differences in the change of parameters of cells under different aging conditions. The main junction CdS/CdTe of the cell was destroyed in the absence of buffer layers close to front and back electrodes. Therefore, the cell with a structure of FTO/MZO/CdS/CdTe/BC/Au demonstrates an optimized stability among solar cells with different configurations, which mean that an efficient back contact layer and a composite front electrode are the indispensable structural element to attain high stability in the CdS/CdTe solar cell. However, the test results also expose that the introduction of the buffer layer between front electrode and CdS is a dialectical consideration. These conclusions not only are conducive to the study on CdTe solar cell stability but also provide a certain experimental basis for standard test and outdoor applications of CdTe solar cell.

Data Availability

The data used to support the findings of this study are available from the corresponding author upon request.

Conflicts of Interest

The authors declare that they have no conflicts of interest.

Acknowledgments

The authors would acknowledge the Science and Technology Project supported by the Sichuan Provincial Human Resources and Social Security Department, the School-Enterprise Cooperation Project (17H0242) supported by the Chuzhou MART Smart New Materials Technology Co., Ltd., the 8th New Century Higher Education Teaching Reform Research Project of Sichuan University, the Quality and Teaching Reform Project of Higher Education Talents in Sichuan Province from 2018 to 2020, and the Fundamental Research Funds for Central Universities.

References

[1] International Electrotechnical Commission, *Terrestrial Photovoltaic (pv) Modules - Design Qualification and Type Approval - Part 2: Test Procedures*, IEC, Geneva, Switzerland, 2016.

[2] D. C. Jordan, C. Deline, S. R. Kurtz, G. M. Kimball, and M. Anderson, "Robust PV degradation methodology and application," *IEEE Journal of Photovoltaics*, vol. 8, no. 2, pp. 525–531, 2018.

[3] C. R. Osterwald and T. J. McMahon, "History of accelerated and qualification testing of terrestrial photovoltaic modules: a literature review," *Progress in Photovoltaics: Research and Applications*, vol. 17, no. 1, pp. 11–33, 2009.

[4] T. H. Myers, S. W. Edwards, and J. F. Schetzina, "Optical properties of polycrystalline CdTe films," *Journal of Applied Physics*, vol. 52, no. 6, pp. 4231–4237, 1981.

[5] M. A. Green, Y. Hishikawa, E. D. Dunlop, D. H. Levi, J. Hohl-Ebinger, and A. W. Y. Ho-Baillie, "Solar cell efficiency tables (version 51)," *Progress in Photovoltaics: Research and Applications*, vol. 26, no. 1, pp. 3–12, 2018.

[6] I. Rimmaudo, A. Salavei, E. Artegiani et al., "Improved stability of CdTe solar cells by absorber surface etching," *Solar Energy Materials and Solar Cells*, vol. 162, pp. 127–133, 2017.

[7] N. R. Paudel, K. A. Wieland, M. Young, S. Asher, and A. D. Compaan, "Stability of sub-micron-thick CdTe solar cells," *Progress in Photovoltaics: Research and Applications*, vol. 22, no. 1, pp. 107–114, 2014.

[8] M. Nardone and D. S. Albin, "Degradation of CdTe solar cells: simulation and experiment," *IEEE Journal of Photovoltaics*, vol. 5, no. 3, pp. 962–967, 2015.

[9] D. Guo, D. Brinkman, A. R. Shaik, C. Ringhofer, and D. Vasileska, "Metastability and reliability of CdTe solar cells," *Journal of Physics D: Applied Physics*, vol. 51, no. 15, article 153002, 2018.

[10] A. W. Czanderna and F. J. Pern, "Encapsulation of PV modules using ethylene vinyl acetate copolymer as a pottant: a critical review," *Solar Energy Materials and Solar Cells*, vol. 43, no. 2, pp. 101–181, 1996.

[11] T. J. McMahon, "Accelerated testing and failure of thin-film PV modules," *Progress in Photovoltaics: Research and Applications*, vol. 12, no. 23, pp. 235–248, 2004.

[12] K. D. Dobson, I. Visoly-Fisher, G. Hodes, and D. Cahen, "Stability of CdTe/CdS thin-film solar cells," *Solar Energy Materials and Solar Cells*, vol. 62, no. 3, pp. 295–325, 2000.

[13] D. S. Albin, "The correlation of capacitance-voltage hysteresis measurements with performance during accelerated lifetime testing of polycrystalline thin film solar cells," in *2010 17th IEEE International Symposium on the Physical and Failure Analysis of Integrated Circuits*, pp. 1–6, Singapore, Singapore, 2010.

[14] S. H. Demtsu, D. S. Albin, J. W. Pankow, and A. Davies, "Stability study of cds/cdte solar cells made with ag and ni back-contacts," *Solar Energy Materials and Solar Cells*, vol. 90, no. 17, pp. 2934–2943, 2006.

[15] D. S. Albin, R. G. Dhere, S. C. Glynn, J. A. del Cueto, and W. K. Metzger, "Degradation and capacitance: voltage hysteresis in cdte devices," in *Reliability of Photovoltaic Cells, Modules, Components, and Systems II*, pp. 741201–741212, San Diego, CA, USA, 2009.

[16] C. Deline, J. del Cueto, D. S. Albin, and S. Rummel, "Metastable electrical characteristics of polycrystalline thin-film photovoltaic modules upon exposure and stabilization," *Journal of Photonics for Energy*, vol. 2, no. 1, article 022001, 2012.

[17] X. Wu, J. Zhou, A. Duda et al., "Phase control of Cu_xTe film and its effects on CdS/CdTe solar cell," *Thin Solid Films*, vol. 515, no. 15, pp. 5798–5803, 2007.

[18] L. L. Wu, L. H. Feng, W. Li et al., "Effect of ZnTe/ZnTe:Cu complex back-contact on device characteristics of CdTe solar cells," *Science in China Series E: Technological Sciences*, vol. 50, no. 2, pp. 199–205, 2007.

[19] S. Ren, H. Li, C. Lei et al., "Interface modification to enhance electron extraction by deposition of a ZnMgO buffer on SnO_2-coated FTO in CdTe solar cells," *Solar Energy*, vol. 177, pp. 545–552, 2019.

[20] J. M. Kephart, A. Kindvall, D. Williams et al., "Sputter-deposited oxides for interface passivation of CdTe photovoltaics," *IEEE Journal of Photovoltaics*, vol. 8, no. 2, pp. 587–593, 2018.

[21] J. D. Major, R. E. Treharne, L. J. Phillips, and K. Durose, "A low-cost non-toxic post-growth activation step for CdTe solar cells," *Nature*, vol. 511, no. 7509, pp. 334–337, 2014.

[22] Y. Y. Proskuryakov, K. Durose, J. D. Major et al., "Doping levels, trap density of states and the performance of co-doped CdTe(As,Cl) photovoltaic devices," *Solar Energy Materials and Solar Cells*, vol. 93, no. 9, pp. 1572–1581, 2009.

[23] S. S. Hegedus and W. N. Shafarman, "Thin-film solar cells: device measurements and analysis," *Progress in Photovoltaics: Research and Applications*, vol. 12, no. 23, pp. 155–176, 2004.

[24] V. P. Singh, D. L. Linam, D. W. Dils, J. C. McClure, and G. B. Lush, "Electro-optical characterization and modeling of thin film CdS–CdTe heterojunction solar cells," *Solar Energy Materials and Solar Cells*, vol. 63, no. 4, pp. 445–466, 2000.

[25] A. E. Rakhshani, "Heterojunction properties of electrodeposited CdTe/CdS solar cells," *Journal of Applied Physics*, vol. 90, no. 8, pp. 4265–4271, 2001.

Hindawi
International Journal of Photoenergy
Volume 2019, Article ID 1674134, 12 pages
https://doi.org/10.1155/2019/1674134

Research Article

Interaction of Vibration and Air Flow-Accelerating Droplet Emission from the Gas Diffusion Layer of Proton Exchange Membrane Fuel Cell

Sitong Chen,[1,2] **Xueke Wang**,[3] **Tong Zhu**,[1] **and Xiaofeng Xie**[2,4]

[1]*School of Mechanical Engineering and Automation, Northeastern University, Shenyang, 110819 Liaoning, China*
[2]*Institute of Nuclear and New Energy Technology, Tsinghua University, Beijing 100084, China*
[3]*Beijing Institute of Space Launch Technology, Beijing 100076, China*
[4]*Shanxi Research Institute for Clean Energy, Tsinghua University, Taiyuan 030032, China*

Correspondence should be addressed to Tong Zhu; tongzhu_neu@126.com and Xiaofeng Xie; 1043076102@qq.com

Received 28 September 2019; Accepted 24 October 2019; Published 10 December 2019

Guest Editor: Liang Chu

In order to explore the influence of vibration that the vehicles are often subjected on water management of PEMFC, the dynamic characteristics of vibrating droplet on gas diffusion layer (GDL) surface were investigated through a high-speed image technology. The operating condition of vertical and horizontal excitations separately or coupled with air flow under different frequencies and amplitudes are applied on the substrate, so that the laws for the transition from Wenzel-Cassie regime to Cassie regime and the contact angle, the deformation rate for the width and height are obtained. It is observed that the wetting diameter of the droplet is smaller than the initial value under vertical vibration, making it easier for the gas to discharge the water droplets from the PEMFC. For the horizontal excitation, the droplet is pulled apart when the applied energy exceeded the cohesive energy at elevated frequency and amplitude. Moreover, as to the interaction of vibration and air flow, the droplet was more likely to move forward under the gas-driven force.

1. Introduction

With the steady promotion of public awareness on environmental protection and sustainable development, fuel cells will become the major power options to replace the traditional fossil energy in the future. Among all kinds of fuel cells, the proton exchange membrane fuel cell (PEMFC) has a very wide range of application in military and civil fields, such as aerospace industry, deep-sea submarines, stationary and portable power sources, or transportation sector, because it offers low operating temperatures, high energy conversion efficiency, rapid cold start-up, no pollution, long service life, and compact structure [1, 2]. As an alternative vehicular power train, the PEMFC has extensive market prospect in automotive application, the world's major car manufacturers in recent years have launched their new PEMFC models. From 2013 to the end of 2017, the PEMFC passenger cars' global sales totaled 6,475 vehicles, 3,382 of which were sold in 2017, accounting for 52.23% of the total sales [3].

In the actual road conditions, the PEMFCs in vehicles are often subjected to the harsh dynamic situations accompanied with mechanical vibration and shock. Passenger vehicles generally experience vibrations in the range of 8-16 Hz due to the unevenness of the road and the oscillation of the axel and wheel with the suspension system [4]. The long-term vibration behaviors may cause and exacerbate the defects of PEMFC components, such as pinholes, cracks, and delamination, having influence on the performance, durability, and reliability of the PEMFC stack [5, 6]. Therefore, the effect and function mechanism of vibrations on PEMFCs have gained more and more attention from researchers, mainly by means of experiments and numerical simulations for further insight.

Rajalakshmi et al. [7] subjected a 500 W PEMFC stack to shocks, random and swept-sine excitations by using a

Table 1: The experimental operating conditions.

Current density (mA/cm^2)	Temperature (°C)	Stoichiometry (air/H_2)	Relative humidity (air/H_2)
300	65	2/1.2	0/0

vibrating platform at various frequencies and different acceleration in three axe directions. The electrochemical performance of the stack is in good agreement before and after the vibration and shock tests, showing the mechanical integrity of the system, and a posttesting stack inspection shows a minor compression force release at the bolts. Diloyan et al. [8] experimentally investigated the effect of different constant mechanical vibration conditions on platinum particle agglomeration and growth in the catalyst layer of a Membrane Electrode Assembly (MEA) for a PEMFC with a 25 cm^2 active surface area. By using 300 h accelerated tests and transmission electron microscopy (TEM), they came to the conclusion that the average diameter of Pt particles under vibration is 10% smaller than the ones without vibration conditions. Hou et al. [9–13] conducted a series of long-term strengthened road vibration studies on PEM fuel cell stack with a road simulation test bench and a six-channel multiaxial simulation table. They analyzed and determined the negative changes in gas tightness, electrical insulation, characteristic parameters (open circuit voltage V_0, Tafel slope b, and ohmic resistance R), steady-state efficiency, and hydrogen utilization, as well as performance degradation of the fuel cell stack in detail.

Another part of related studies in the published works is mainly focused on numerical simulations. Ahmed et al. [14] developed a three-dimensional finite element model of a PEMFC for the free vibration analysis. They modelled the PEMFC as a laminated composite plate composed of a membrane, gas diffusion electrodes, and bipolar plates and then investigated the relationship between natural frequency and material thickness, Young's modulus, and density for each component layer. Banan et al. [15] established a two-dimensional model based on the cohesive element approach to predict the delamination and crack evolution at the membrane/catalyst layer interface in PEMFCs. After a parametric study, they found the effects of amplitude and frequency of applied vibrations as well as initial delamination length on damage propagation. Al-Baghdadi [16] created a model about the natural frequencies and mode shapes of the PEM fuel cell stack to discuss how the natural frequency varies as a function of material properties and thickness of the stack components, number of cells, and misalignment during assembly process under a vibration environment.

However, the transport of liquid water under vibration conditions in PEMFCs remains an area of research in progress. Breziner et al. [17] failed to run a custom-made fuel cell stack with a clear window in the cathode side and replaced it with a commercial, 36 cm^2 single cell to investigate the influence exerted by frequency and acceleration of vibration on the overall fuel cell performance. They conjectured that the decay could be due to an alteration of water transport in the MEA. Santamaria et al. [18] experimentally characterized water droplet motion and adhesion on GDL materials in the presence of vibration. They designed a simplified experimental setup to consider only GDL and liquid interface effects. Moreover, they concluded that vibration leads to liquid redistribution that causes an increased wetting diameter and reduced height, resulting in up to a 15% higher net force required for removing water from PEFC GDL materials. Sellman and Santamaria [19] on this basis added a single Lexan channel mounted on the vibration stage to simulate two-phase flow. The results show that flow-channel detachment velocity is increased for higher vibration scenarios potentially due to altered droplet aerodynamics and net adhesion force. This work uses ex situ experimental techniques to progressively investigate the dynamic characteristics of vibrating droplet on GDL surface under vertical and horizontal excitations separately or coupled with air flow through high-speed image technology, which is motivated by the performance fluctuation of the PEMFC from the in situ experiment.

2. Experimental Methods and Apparatus

At first, an in situ experiment was performed to investigate the effect of PEMFC performance under mechanical vibration. As to the PEMFC, a commercially available Nafion® 211 membrane with an active area of 25 cm^2 and SGL-25BC carbon papers of which the porosity was 80% and the air permeability was 1.0 cm^3/(cm^2·s) were chosen. The Pt catalyst loading of both cathode and anode sides was 0.5 mg cm^{-2}. For under the vibrational frequency of 25 Hz, the amplitude of 2.5 mm and the PEMFC operating conditions are summarized in Table 1; after repetitive tests, a sudden rise in cell voltage while loading vibration was obtained. According to this law, the influence of vibration on the performance of the vehicle stack will be more obvious under the condition of a large area and multiple cells. Therefore, we designed an ex situ test platform with an image acquisition system to explore the critical condition of the vibrating droplet on GDL surface.

2.1. Experimental Setup. The image acquisition system consists of a high-speed camera (OLYMPUS i-SPEED TR), a macro lens (OLYMPUS SZ61), an auxiliary light, and a computer. The high-speed camera is equipped with a macro lens so as to collect clearer real-time images, as is displayed in Figure 1(a). There are two kinds of light sources employed in this test shown in Figures 1(b) and 1(c): one is the halogen light source, as the backlight for observing the dynamic behavior of vibrating droplet on GDL surface, can avoid the uneven color distribution caused by photochromatic migration. The other is the LED light (LG-150E), serving as a reflection light source. The vibration generator can provide horizontal excitations and vertical excitations in

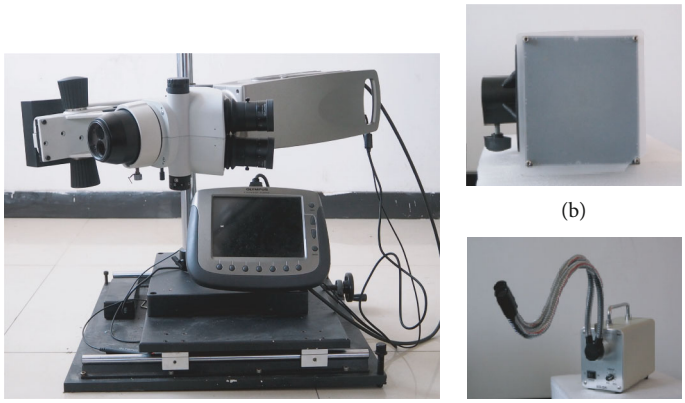

(a) (b) (c)

Figure 1: The photographs of the high-speed camera and light source.

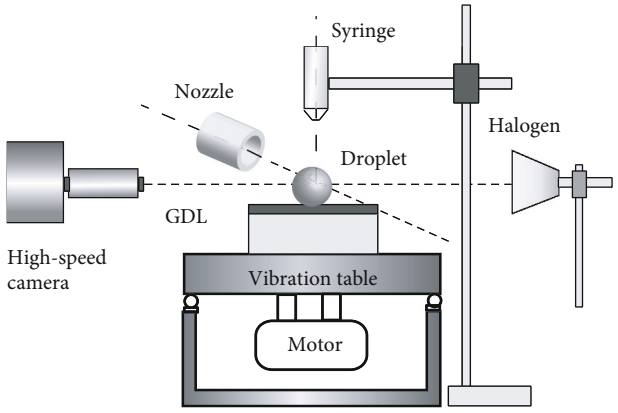

Figure 2: The schematic diagram of droplet vibration experiment.

the frequency range from 1 Hz to 600 Hz with the maximum displacement of 5 mm, capable of acceleration amplitude up to 20 g. It can be used to simulate the real vehicle vibration frequencies ranging from 17 Hz to 40 Hz with the maximum amplitude of 0.95 g during its operation [20, 21]. In this paper, each experiment was repeated three times under stable test condition control to avoid accidental phenomena.

2.2. Description of the Experimental Test Platform. Figure 2 exhibits the schematic diagram of the droplet vibration tests which were realized by using the vibration generator, the image acquisition system, and the mass flow controller. The GDL substrate was tightly seated to the vibration generator and illuminated by a cold light source with a high-speed camera mounted opposite to record the movement of water droplet under vibration conditions. In view of the diameter of water droplets in the gas flow channels of PEMFC which was usually between 0.6 mm and 1 mm, we used a pipettor to put the deionized water droplet on the surface of GDL and fixed a nozzle 2 mm away from the droplet with a diameter of 0.8 mm, which was connected to the mass flow meter in order to control the gas flow rate.

3. Results and Discussion

Due to the strong hydrophobicity of the diffusion layer surface in PEMFC, the water generated by the reaction exists in the form of droplets on the GDL. From Figure 3(a), the droplets will present different contact forms for the low surface flatness and the uneven distribution of PTFE as well as different pore structures of GDL. Figure 3(b) shows the infiltrating state of the droplets on the rough surface, which are the Wenzel regime, the Cassie regime, and the Wenzel-Cassie regime, respectively [22, 23]. The water produced by PEMFC breaks through the GDL and reaches the surface, which exists briefly in the regime of Wenzel, and then, the droplets will be in the form of Wenzel-Cassie [19]. As to a droplet in the Wenzel-Cassie regime, it receives the vibration energy E_k, the adhesion power between the droplet and GDL surface E_a, and the cohesion force E_r generated when the droplet is stretched.

For a vibration device with vibrational frequency f and amplitude A, the energy transmitted to the droplet through the vibration is given as follows [24]:

$$E_{ko} \propto \frac{1}{2}\rho V(2\pi f A)^2. \quad (1)$$

The kinetic energy transferred to the droplet by vibration is as follows:

$$E_k = k \cdot \frac{1}{2}\rho V(2\pi f A)^2, \quad (2)$$

where k is the energy transfer efficiency, ρ is the density of the droplet, V is the volume of the droplet, f is the vibrational frequency, and A is the amplitude. It is necessary to overcome the adhesion power between the droplet and solid surface to realize the transition of the droplet state on GDL surface:

$$E_a = \gamma_{1v}(1 + \cos\theta)\Delta A. \quad (3)$$

When $E_k < E_a$, the droplet cannot change from the Wenzel-Cassie regime to the Cassie regime, while $E_r > E_k >$

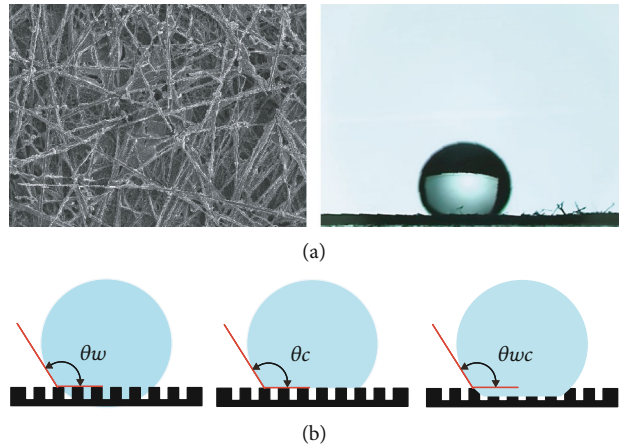

(a)

(b)

Figure 3: (a) The carbon paper and droplet and (b) different contact patterns of droplet on the GDL.

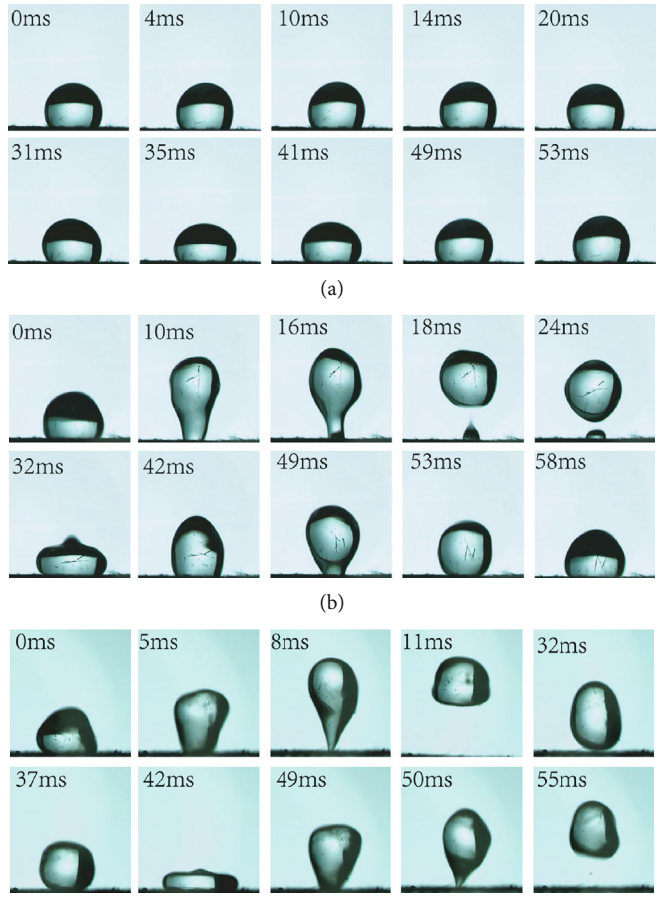

(a)

(b)

(c)

Figure 4: Under the vertical vibration frequency of 20 Hz, different amplitude conditions, the movement of droplets on the surface of GDL.

E_a, the droplet starts the transition from the Wenzel-Cassie regime to the Cassie regime.

3.1. Dynamic Performance of the Droplet under Vertical Vibration. It was found in the experiment that as the vibration amplitude increased, there were three different situations when the vertical vibration at a certain value of frequency was applied to the surface of GDL. In Figure 4(a), the vibration deformation of the droplet on GDL was too small to start the transition from the Wenzel-Cassie regime to the Cassie regime while the input frequency was 20 Hz and the amplitude was 1 mm. Keeping the same frequency and gradually increasing the amplitude to 2 mm, the droplet would be snapped during oscillation, leaving a trail behind. As shown

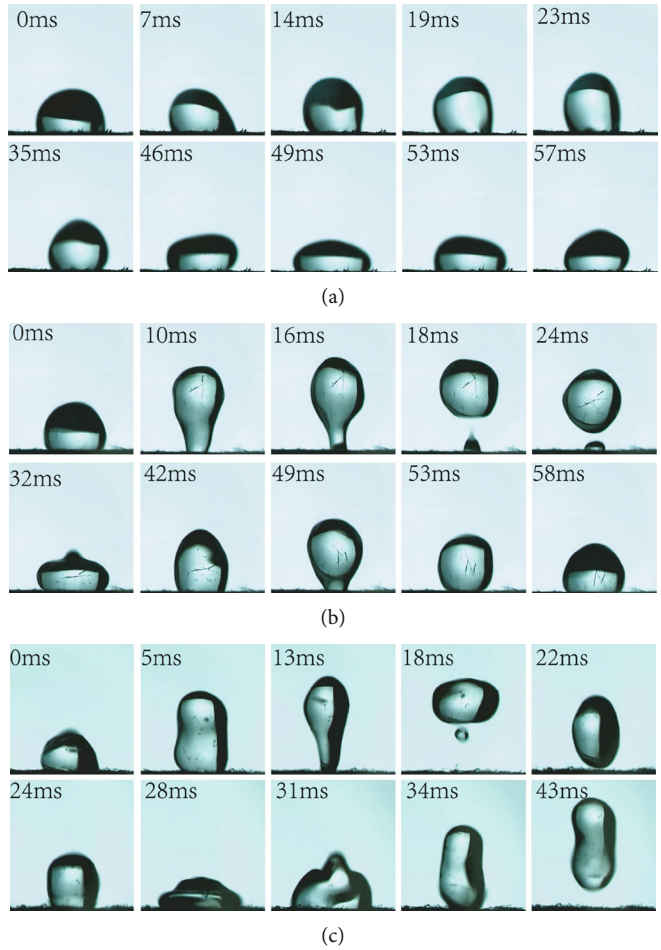

Figure 5: Under the vertical vibration amplitude of 2 mm, different frequency conditions, the movement of droplets on the surface of GDL.

in Figure 4(b), after falling back to the GDL surface, the droplet could not break away again for cyclic motion. It can be observed from Figure 4(c) that when the amplitude was increased to 2.5 mm, the vibrational energy of the droplet could overcome the adhesion power between droplet and GDL surface so that the droplet was completely separated from the gas diffusion layer to achieve the transition from the Wenzel-Cassie regime to the Cassie regime.

If the vibration amplitude remained unchanged and the frequency was variate, the vibrating mode of the droplet had the similar variation trend as that under the same frequency. From Figure 5, it can be found that after vibrating at an amplitude of 2 mm and the frequencies added from 15 Hz to 30 Hz, the vibration of the droplet became apparent and the droplet accomplished the transition from the Wenzel-Cassie regime to the Cassie regime at a larger frequency. For the water management of the PEMFC, Figures 4(c) and 5(c) are ideal state as the droplets completely bounced off the GDL surface and were easily blown away under a small gas flow rate.

The deformation rate is a parameter to quantitatively measure the deformation extent of the droplet with time. In this work, the gradient of the wetting diameter D/D_0 and the height H/H_0 during the droplet vibration were analyzed in real time, where D_0, D, H_0, and H represent the wetting diameter and height of the droplet at rest or under vibration, respectively. Figure 6(a) shows the maximum height of the droplet increasing with the augmentation of amplitudes, and the droplet height presents a periodical change with the cycle of vibrating motion at a constant frequency of 20 Hz. When the amplitude was 1 mm, the height of the droplet deformed little, while the droplet being vibrated at an amplitude of 2 mm, its height reached two different maximum values, which were $1.8\,h_0$ and $1.6\,h_0$ within 60 ms. The peak value came up to $3.0\,h_0$ with the amplitude added to 2.5 mm. Furthermore, there was a correspondence between the gradient of the wetting diameter and the height of the droplet. When the wetting diameter reached the maximum value, the corresponding height of the droplet was the minimum as shown in Figure 6(b).

To observe how the frequencies influence the wetting diameter and the height of the droplet at a constant amplitude of 2 mm, the results of the experiments are exhibited in Figure 7. The maximum of the droplet height gradually rises along with the increase of frequency; also, the vibrational frequencies of the droplet were different under various driving frequencies. When the driving frequency was 15 Hz, which was basically consistent with the vibrational frequency, the

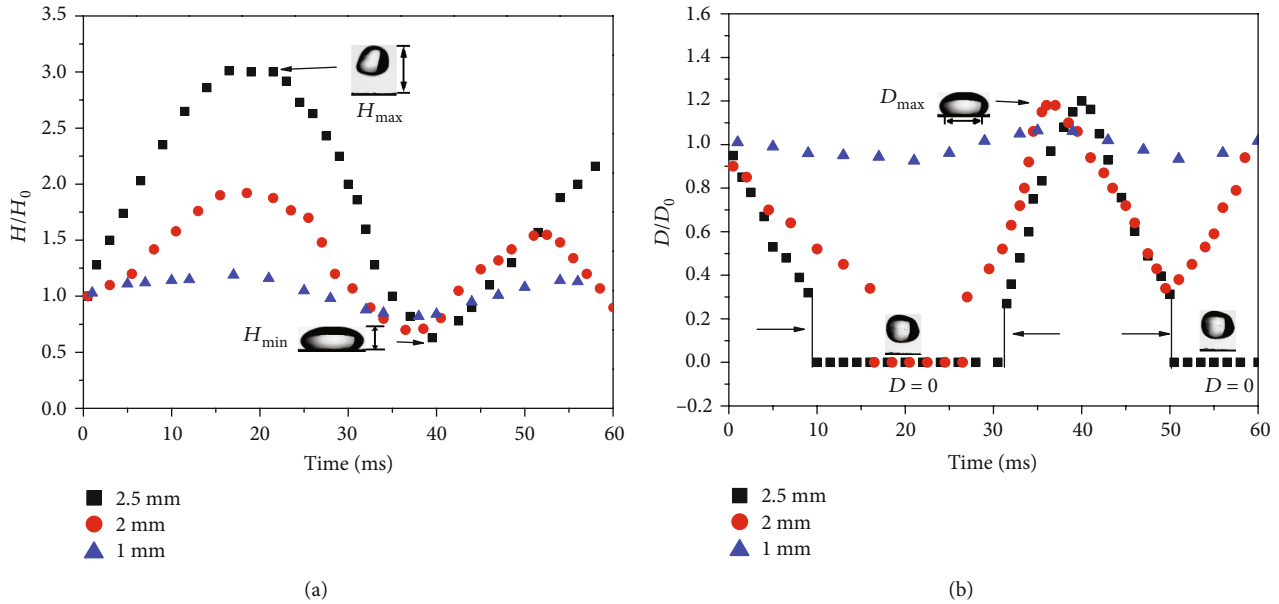

Figure 6: The change rate of the droplet with time under different amplitudes: (a) height of droplet and (b) wetting diameter of droplet.

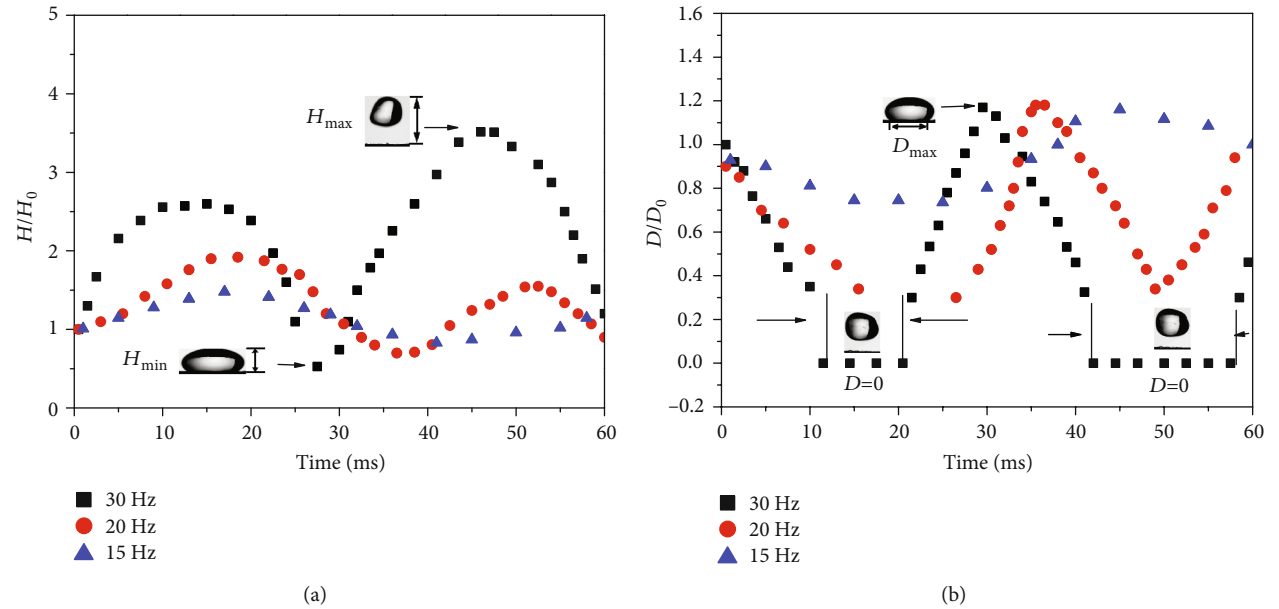

Figure 7: The change rate of the droplet with time under different frequencies: (a) height of droplet and (b) wetting diameter of droplet.

droplet always contacted with the GDL surface. With the rise of driving frequency to 20 Hz and 30 Hz, the wetting diameter was decreased to 0 during 11-27 ms and 12-20, 43-58 ms so that the vibrational frequencies were corresponding to 22 Hz (T = 45 ms) and 32 Hz (T = 31 ms), different from the driving frequencies.

The gradient of the maximum height of droplet under different frequencies was obtained by calculating the average value of the maximum height of droplet in three cycles under various frequencies and amplitudes. As shown in Figure 8, the gradient of the droplet height increased with the augmentation of frequency at the same amplitude, especially under large amplitude (2.5 mm), and the gradient of the maximum height of droplet enhanced rapidly. When the vibrational frequency was greater than 15 Hz and the amplitude was 2.5 mm, the droplet was separated from the surface of GDL. When the frequency was greater than 20 Hz and the amplitude was 2 mm, the droplet broke away from the GDL surface.

3.2. Dynamic Performance of the Droplet under Horizontal Vibration. Under a constant horizontal frequency of 20 Hz from Figure 9, it can be seen that while the amplitude was increased to 2 mm, the droplet showed a tendency of fracture

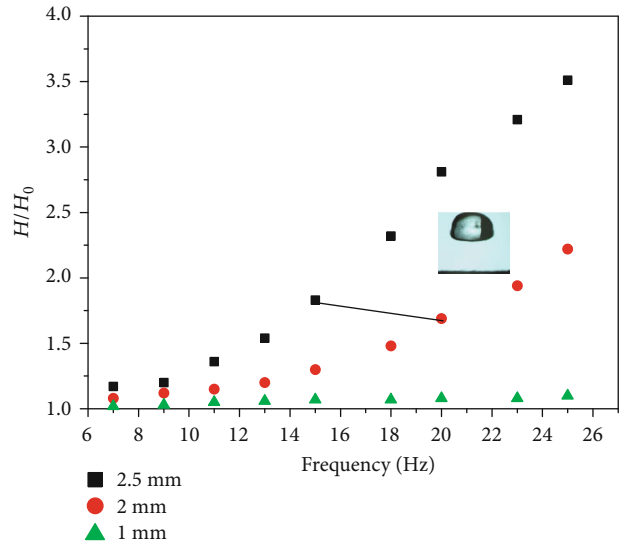

FIGURE 8: The maximum gradient of droplet height at different frequencies.

at 10 ms and left a water film on the surface of GDL, stretching the wetting diameter between the droplet and GDL surface longer. With the rise of amplitude to 2.5 mm in Figure 9(c), the droplet would be snapped during the expansion, leaving a trail, because the bottom of the droplet was still attached to the micropores of the GDL due to its viscosity and the applied energy exceeded the cohesive energy of the droplet so that the droplet was pulled off to form a new small droplet. For an 8 μL droplet, keeping the same amplitude at 2 mm and inputting a changing vibrational frequency (less than 7 Hz), the variation trend was similar as the case above, as shown in Figure 10.

The static contact angle of the droplet changes under the condition of horizontal vibration. The contact angle corresponding to the front contact point is known as the advancing contact angle θ_A, and that corresponding to the rear contact point is called the receding contact angle θ_B. The difference between the advancing contact angle and the receding contact angle (θ_A-θ_B) is contact angle hysteresis.

Figure 11 exhibits the periodic changes of the advancing contact angle (θ_A) and the receding contact angle (θ_B). As the vibration moved to the right from the equilibrium position, the advancing contact angle of the droplet increased gradually and reached the maximum value of 172° when the vibration arrived at the far-right end. Accordingly, the receding contact angle decreased gradually to the minimum value of 80° and the contact angle hysteresis (θ_A-θ_B) gradually enhanced in the process just as 0-17 ms in Figure 11(b). As mentioned above, the wetting diameter of the droplet became larger so that the adhesion force between the droplet and GDL rose up. Therefore, even if the contact angle of the droplet increased to the maximum, the droplet did not scroll on the GDL. When the vibration moved from the far-right end to the far-left end, the advancing contact angle of the droplet gradually decreased to the minimum value of 76°, but the receding contact angle gradually enhanced to the maximum value of 165°. While the advancing contact angle reduced to equal to the receding contact angle, the droplet was in the equilibrium position. At this point, the wetting diameter of the droplet was smallest and the height was largest.

Under a larger amplitude, the shape of the droplet changed significantly so that the advancing contact angle and the receding contact angle of the droplet could not be measured accurately. Therefore, the shape of the droplet was represented by its wetting diameter. Figure 12 shows the variation of the droplet wetting diameter with time under the frequency of 20 Hz and the amplitude of 2 mm as well as 2.5 mm. The wetting diameter of the droplet changed irregularly with the vibration. When the amplitude was 2 mm, the wetting diameter of the droplet was larger than the initial diameter. There were more water molecules entering the micropores of the GDL, adding the adhesion force between the droplet and GDL. With the augmentation of the amplitude to 2.5 mm, the wetting diameter of the droplet gradually decreased in the initial stage. At 21 ms, the droplet was pulled apart to form a small droplet which vibrated in the new position and after that, the wetting diameter first decreased and then increased.

Figure 13 clearly indicates the displacement of the droplet central point varying with time under different amplitudes. With the rise of amplitude, the maximum displacement of the droplet gradually increased and the displacement of the droplet increased and decreased correspondingly with the recirculation of the vibration in the horizontal direction. At the amplitude of 1 mm, the maximum displacement in the positive direction was close to that in the negative direction, both of which were 0.5 mm. It indicated that the droplet did not slip on the GDL surface. When the amplitude increased to 2 mm, the positive displacement (1.4 mm) of the droplet central point was greater than the negative displacement (0.6 mm) so that the droplet slid. As the amplitude added up to 2.5 mm, the droplet fractured at 21 ms and then the formed droplet would reciprocate in the new equilibrium position.

3.3. Dynamic Performance of the Air Flow-Induced Droplet under Vibration. Above all, several experiments about the dynamic performance of the air flow-induced droplet without vibration were performed. The movement of the 8 μL water droplet on GDL surface at different air velocities of 2.76 m/s, 3.39 m/s, 3.9 m/s, and 4.52 m/s is shown in Figure 14. From Figures 14(a) and 14(b), it can be observed that at a low gas flow rate, the receding contact angle of the droplet gradually decreased and the advancing contact angle gradually increased over time, because the force that the gas put on the droplet was less than the adhesion force between the droplet and GDL, which prevented the droplet from leaving the GDL surface and formed a small water film. As the flow rate increased to 3.9 m/s, the tail of the droplet was stretched as shown in Figure 14(c). When the flow rate reached 4.52 m/s, the drag force of the gas made the droplet forming a slender column, the front of the droplet contacted with the GDL, and the tail was suspended in the air. At this moment, although the drag force was not enough to overcome the adhesion force between the droplet and GDL, it

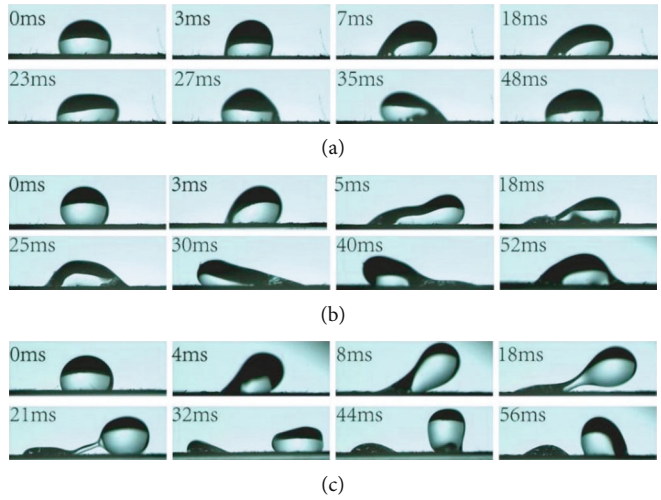

Figure 9: Under the horizontal vibration frequency of 20 Hz, different amplitude conditions, the movement of droplets on the surface of GDL.

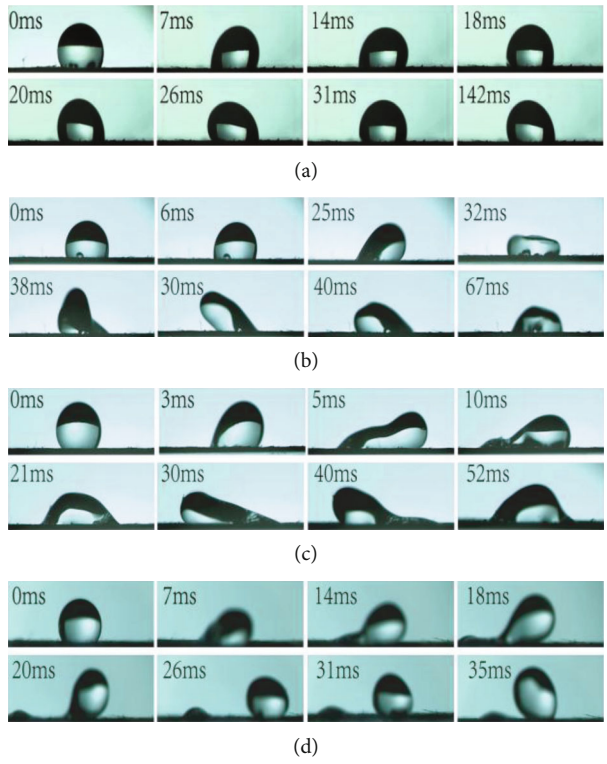

Figure 10: Under the horizontal vibration amplitude of 2 mm, different frequency conditions, the movement of droplets on the surface of GDL.

exceeded the cohesion force of the droplet so that the droplet suspended in the air was pulled apart.

To discuss the motion characteristics of the droplets with different volumes on GDL surface, the droplets of 6 μL, 8 μL, and 10 μL at the air velocity of 5 m/s were investigated in Figure 15. The 6 μL droplet completely broke away from the GDL, and the bottom of the 8 μL and 10 μL droplets fractured and migrated on the surface of GDL. In addition, the wetting diameter of the 10 μL droplet was larger compared with the 8 μL droplet. This was because the gravity and adhesion force of the droplet tiny in size were small, and the force of the gas could overcome the adhesion force and gravity of the droplet under a larger gas flow rate, making the droplet float above the GDL.

Furthermore, the surface properties of the GDL also affect the movement of the droplet. Figure 16 shows the

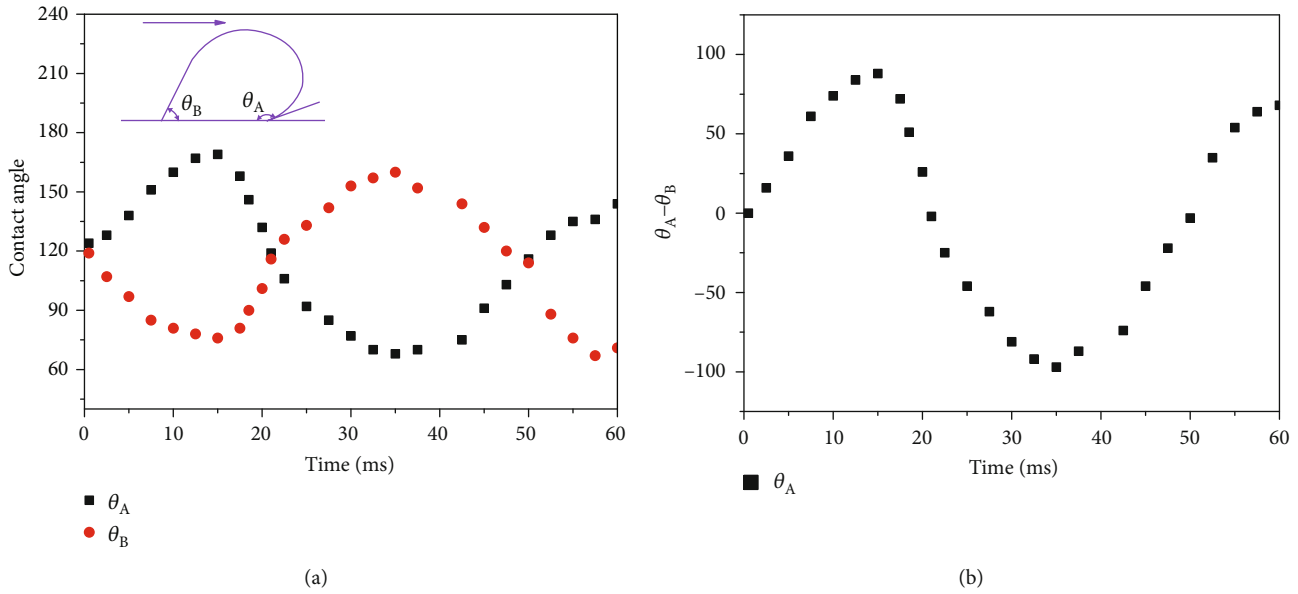

FIGURE 11: The variation of the droplet with time at the frequency of 20 Hz and the amplitude of 1 mm: (a) contact angle and (b) contact angle hysteresis.

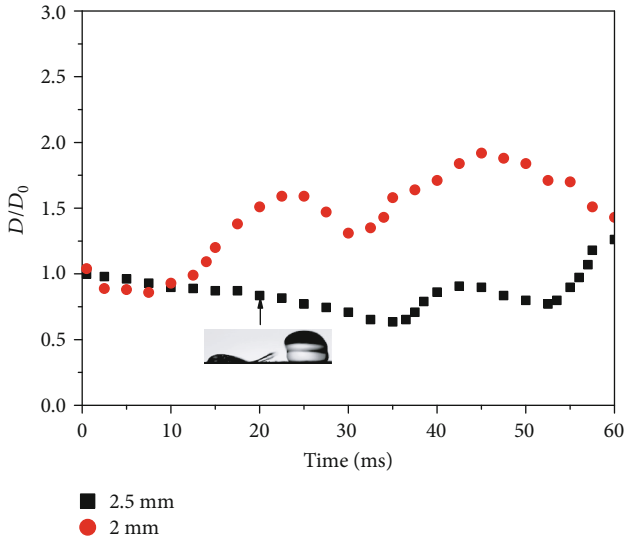

FIGURE 12: The variation of the droplet wetting diameter with time under different amplitudes.

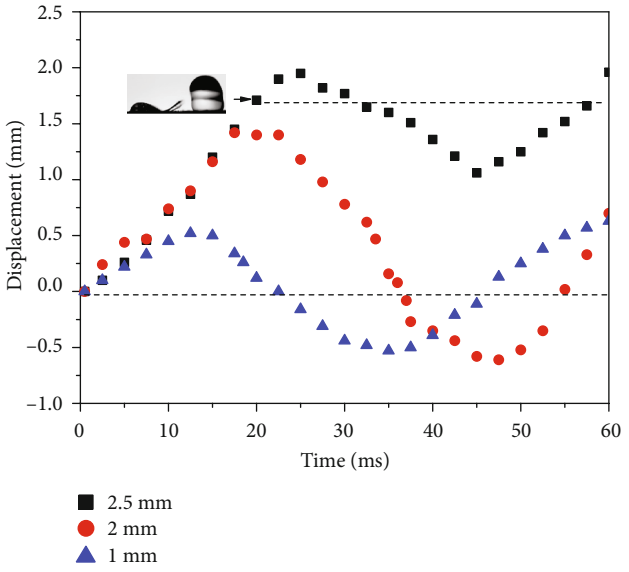

FIGURE 13: The variation of the droplet displacement with time.

movement of the 6 μL droplet on the surface of dry or wet GDL at the gas flow rate of 5 m/s. On the dry GDL surface, the bottom of the droplet separated from the GDL under the gas-driven force and moved forward. While on the wet GDL surface, the contact angle of the droplet became smaller and the wetting diameter as well as the adhesion force of the droplet increased, making it difficult for the droplet to break away from the GDL surface. The droplet was elongated and fractured under the gas-driven force, forming several small droplets on the GDL surface.

Taking the vibration into account, the direction of the vibration is also an important factor to the movement of the droplet. Figure 17 shows the movement of the 6 μL droplet on GDL surface under the interaction of vertical vibration and air flow at a frequency of 20 Hz and an amplitude of 1.5 mm. According to the above analysis, the droplet could not start the transition from the Wenzel-Cassie regime to the Cassie regime under this condition, but the height of the droplet changed. The gas flow rate was 2 m/s, less than the critical velocity of the water droplet. It can be seen from the picture that the droplet could not break away from GDL under the gas-driven force in the first 20 ms. After 34 ms, the vibration provided an upward force for the droplet to be stretched, the wetting diameter between the droplet and

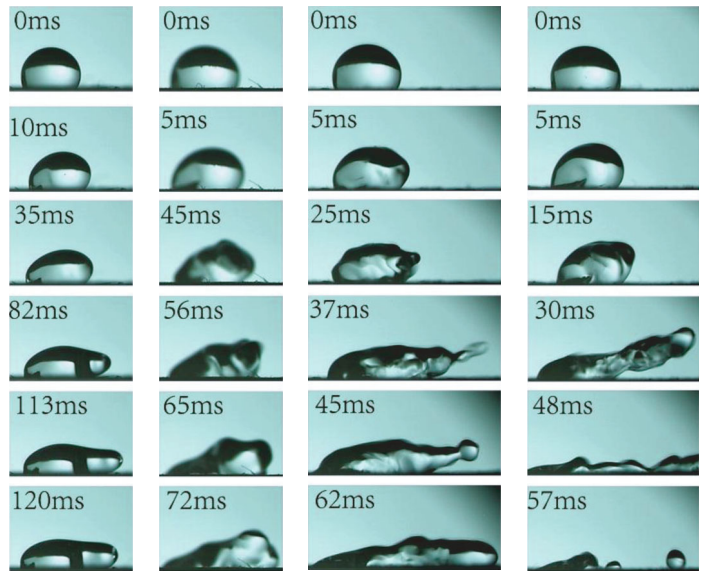

Figure 14: The movement of 8 μL droplet on GDL surface under different air velocities.

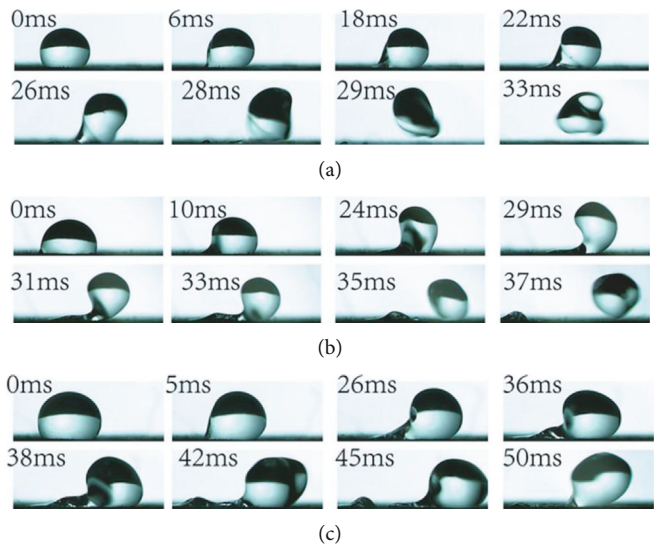

Figure 15: The movement of different volume droplets on GDL surface at air velocity of 5 m/s.

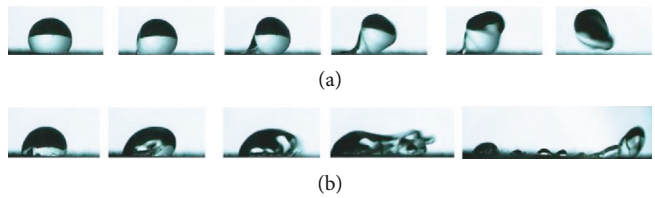

Figure 16: The movement of droplets on the surface of dry or wet GDL at air velocity of 5 m/s.

GDL became shorter, and the height of the droplet increased. At the same time, the gas-driven force on the droplet enhanced so that the droplet bounced off the GDL surface at 74 ms. It should be pointed out that when the vibration provided a downward force to the droplet, the height of the droplet decreased while the contact line and the adhesion force became larger; meanwhile, the gas-driven force reduced, making it difficult for the droplet to break away

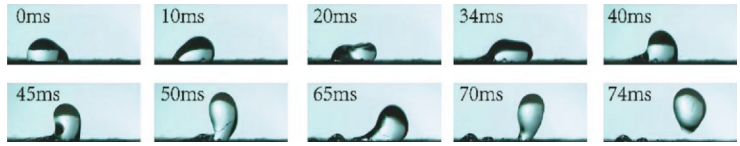

Figure 17: The movement of 6 μL droplet on GDL surface under the interaction of vertical vibration and air flow.

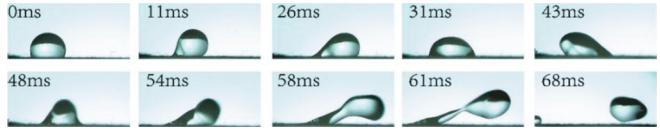

Figure 18: The movement of 8 μL droplet on GDL surface under the interaction of horizontal vibration and air flow.

from the GDL. The same thing happened when the droplet stopped vibrating.

The movement of an 8 μL droplet on GDL surface under the interaction of horizontal vibration and air flow at a frequency of 20 Hz and an amplitude of 1 mm was shown in Figure 18. The gas flow rate was 2 m/s, less than the critical velocity of the water droplet. Under the effect of the gas, the contact angle of the droplet changed ($t = 11$ ms); when the vibration was opposite to the direction of the gas-driven force on the droplet, the droplet moved from right to left in the horizontal direction ($t = 43$ ms) and could not overcome the adhesion force to break away from the GDL. When the vibration was in the same direction as the gas-driven force on the droplet, the droplet was elongated ($t = 58$ ms); at 68 ms, the droplet was pulled off and moved forward under the effect of the gas on the surface of GDL.

4. Conclusions

The PEMFCs in vehicles are often subjected to the harsh operation environment accompanied with mechanical vibration in the actual road conditions. In this paper, we designed an ex situ test platform with an image acquisition system to explore the dynamic characteristics of the vibrating droplet on GDL surface. It was found in the study that when the vertical vibration amplitude was 2.5 mm and the frequency was greater than 15 Hz or the amplitude was 2 mm and the frequency was greater than 20 Hz, the droplet was completely separated from the GDL surface to achieve the transition from the Wenzel-Cassie regime to the Cassie regime. The wetting diameter of the droplet was smaller than the initial diameter for a long time during an oscillation cycle, which made it easier for the gas to discharge the droplets from the PEMFC. While the horizontal vibration amplitude was 2.5 mm and the frequency was larger than 20 Hz or the amplitude was 2 mm and the frequency was larger than 30 Hz, the applied energy exceeded the cohesive energy of the droplet in the expansion process, resulting in the droplet being pulled apart. For the amplitude and frequency larger than 1 mm and 10 Hz, the wetting diameter of the droplet enhanced and there would be more water molecules going into the micropores of the GDL. As to the movement of the droplet on GDL surface under the interaction of vibration and air flow, the droplet was easier to move forward under the gas-driven force. At the same time, the wetting diameter of the droplet added up after vibrating, making it necessary to increase the gas flow rate to achieve the purging effect. The content investigated in this paper is a fundamental understanding of the liquid behavior on GDL under mechanical vibration. It has a certain reference value for the water management of PEMFCs in the actual road conditions.

Data Availability

The measured data used to support the findings of this study are included within the article.

Conflicts of Interest

The authors declare that there is no conflict of interest regarding the publication of this paper.

Acknowledgments

The authors would like to thank Professor Xiang Wu in Shenyang University of Technology and Professor Baodan Liu in Institute of Metal Research, Chinese Academy of Sciences, for their invaluable support. This research was supported financially by the Intergovernmental International Scientific and Technological Innovation Cooperation Key Projects (2016YFE0102700), Major Science and Technology Projects of Shanxi Province (20181101006), and the National Natural Science Foundation of China (51573083 and 51425403).

Supplementary Materials

Fig. S1 The photographs of the high-speed camera and light source. Fig. S2: the contact line and contact height of droplet before and after vertical vibration. Fig. S3: the contact line and contact height of droplet before and after horizontal vibration. *(Supplementary Materials)*

References

[1] J. Hahm, H. Kang, J. Baek, H. Lee, and M. Park, "Design of incremental conductance sliding mode MPPT control applied

by integrated photovoltaic and proton exchange membrane fuel cell system under various operating conditions for BLDC motor," *International Journal of Photoenergy*, vol. 2015, Article ID 828129, 14 pages, 2015.

[2] W. Han, D. Chen, Q. Li, W. Liu, H. Chu, and X. Rui, "Ultrafast flame growth of carbon nanotubes for high-rate sodium storage," *Journal of Power Sources*, vol. 439, article 227072, 2019.

[3] Market Research, "Hydrogen fuel cell vehicles-a global analysis, Information Trends," 2018, March 2018, https://www.marketresearch.com/Information-Trends-v4131/Hydrogen-Fuel-Cell-Vehicles-Global-11546086/.

[4] G. R. Watts and V. V. Krylov, "Ground-borne vibration generated by vehicles crossing road humps and speed control cushions," *Applied Acoustics*, vol. 59, no. 3, pp. 221–236, 2000.

[5] Y. Li, D. A. Dillard, S. W. Case et al., "Fatigue and creep to leak tests of proton exchange membranes using pressure-loaded blisters," *Journal of Power Sources*, vol. 194, no. 2, pp. 873–879, 2009.

[6] S. J. Imen and M. Shakeri, "Reliability evaluation of an open-cathode PEMFC at operating state and longtime vibration by mechanical loads," *Fuel Cells*, vol. 16, no. 1, pp. 126–134, 2016.

[7] N. Rajalakshmi, S. Pandian, and K. S. Dhathathreyan, "Vibration tests on a pem fuel cell stack usable in transportation application," *International Journal of Hydrogen Energy*, vol. 34, no. 9, pp. 3833–3837, 2009.

[8] G. Diloyan, M. Sobel, K. Das, and P. Hutapea, "Effect of mechanical vibration on platinum particle agglomeration and growth in polymer electrolyte membrane fuel cell catalyst layers," *Journal of Power Sources*, vol. 214, pp. 59–67, 2012.

[9] Y. Hou, W. Zhou, and C. Shen, "Experimental investigation of gas-tightness and electrical insulation of fuel cell stack under strengthened road vibrating conditions," *International Journal of Hydrogen Energy*, vol. 36, no. 21, pp. 13763–13768, 2011.

[10] Y. Hou, B. Zhou, W. Zhou, C. Shen, and Y. He, "An investigation of characteristic parameter variations of the polarization curve of a proton exchange membrane fuel cell stack under strengthened road vibrating conditions," *International Journal of Hydrogen Energy*, vol. 37, no. 16, pp. 11887–11893, 2012.

[11] Y. Hou, D. Hao, C. Shen, and Z. Shao, "Experimental investigation of the steady-state efficiency of fuel cell stack under strengthened road vibrating condition," *International Journal of Hydrogen Energy*, vol. 38, no. 9, pp. 3767–3772, 2013.

[12] Y. Hou, X. Zhang, X. Lu, D. Hao, L. Ma, and P. Li, "Ac impedance characteristics of a vehicle pem fuel cell stack under strengthened road vibrating conditions," *International Journal of Hydrogen Energy*, vol. 39, no. 32, pp. 18362–18368, 2014.

[13] Y. Hou, D. Hao, J. Shen, P. Li, T. Zhang, and H. Wang, "Effect of strengthened road vibration on performance degradation of pem fuel cell stack," *International Journal of Hydrogen Energy*, vol. 41, no. 9, pp. 5123–5134, 2016.

[14] H. E. U. Ahmed, R. Banan, J. W. Zu, and A. Bazylak, "Free vibration analysis of a polymer electrolyte membrane fuel cell," *Journal of Power Sources*, vol. 196, no. 13, pp. 5520–5525, 2011.

[15] R. Banan, A. Bazylak, and J. Zu, "Effect of mechanical vibrations on damage propagation in polymer electrolyte membrane fuel cells," *International Journal of Hydrogen Energy*, vol. 38, no. 34, pp. 14764–14772, 2013.

[16] M. A. R. Sadiq Al-Baghdadi, "A parametric study of the natural vibration and mode shapes of pem fuel cell stacks," *International Journal of Energy and Environment*, vol. 7, no. 1, pp. 1–22, 2016.

[17] L. Breziner, P. Strahs, and P. Hutapea, "Effect of vibration on the liquid water transport of pem fuel cells," in *ASME 2009 International Mechanical Engineering Congress and Exposition, American Society of Mechanical Engineers*, pp. 17–22, Lake Buena Vista, Florida, USA, November 2009.

[18] A. D. Santamaria, J. Haydu, D. Senft, and J. Riofrio, "Liquid water interactions with PEFC gas-diffusion layers: the effect of vibration," in *Proceedings of the ASME 2015 International Mechanical Engineering Congress and Exposition. Volume 6B: Energy*, pp. 17–22, Houston, Texas, USA, November 2015.

[19] J. T. Sellman and A. D. Santamaria, "Ex-situ probing of PEFC liquid droplet dynamics in the presence of vibration," *International Journal of Hydrogen Energy*, vol. 42, no. 17, pp. 12551–12558, 2017.

[20] S. Yildirim, S. Erkaya, I. Eski, and I. Uzmay, "Noise and vibration analysis of car engines using proposed neural network," *Journal of Vibration and Control*, vol. 15, no. 1, pp. 133–156, 2009.

[21] V. Rouss and W. Charon, "Multi-input and multi-output neural model of the mechanical nonlinear behaviour of a pem fuel cell system," *Journal of Power Sources*, vol. 175, no. 1, pp. 1–17, 2008.

[22] R. N. Wenzel, "Resistance of solid surfaces to wetting by water," *Industrial and Engineering Chemistry Research*, vol. 28, no. 8, pp. 988–994, 1936.

[23] A. B. D. Cassie and S. Baxter, "Wettability of porous surfaces," *Transactions of the Faraday Society*, vol. 40, pp. 546–551, 1944.

[24] J. B. Boreyko and C. H. Chen, "Restoring superhydrophobicity of lotus leaves with vibration-induced dewetting," *Physical Review Letters*, vol. 103, no. 17, article 174502, 2009.